ASSESSING THE FEASIBILITY OF UTILIZING A UAS-BASED POINT CLOUD IN PAVEMENT SMOOTHNESS/ROUGHNESS MEASUREMENT

FINAL PROJECT REPORT

by

Erzhuo Che
Chase Simpson
Fatih Sen

Oregon State University

Sponsorship
PacTrans, Oregon State University

for

Pacific Northwest Transportation Consortium (PacTrans)
USDOT University Transportation Center for Federal Region 10
University of Washington
More Hall 112, Box 352700
Seattle, WA 98195-2700

In cooperation with U.S. Department of Transportation,
Office of the Assistant Secretary for Research and Technology (OST-R)

DISCLAIMER

The contents of this report reflect the views of the authors, who are responsible for the facts and the accuracy of the information presented herein. This document is disseminated under the sponsorship of the U.S. Department of Transportation's University Transportation Centers Program, in the interest of information exchange. The Pacific Northwest Transportation Consortium, the U.S. Government, and matching sponsors assume no liability for the contents or use thereof.

Dr. Che has financial interests in EZDataMD LLC, a company that commercializes the technology related to this research. The conduct, outcomes, or reporting of this research could benefit EZDataMD LLC and could potentially benefit Dr. Che.

.

TECHNICAL REPORT DOCUMENTATION PAGE

1. Report No.	2. Government Accession No.	3. Recipient's Catalog No.
	01784892	

4. Title and Subtitle

ASSESSING THE FEASIBILITY OF UTILIZING A UAS-BASED POINT CLOUD IN PAVEMENT SMOOTHNESS/ROUGHNESS MEASUREMENT

5. Report Date

12/20/2022

6. Performing Organization Code

7. Author(s) and Affiliations

Erzhuo Che; 0000-0001-7664-8098
Chase Simpson; 0000-0001-6394-0479
Fatih Sen

8. Performing Organization Report No.

2021-S-OSU-1

9. Performing Organization Name and Address

PacTrans
Pacific Northwest Transportation Consortium
University Transportation Center for Federal Region 10
University of Washington More Hall 112 Seattle, WA 98195-2700

10. Work Unit No. (TRAIS)

11. Contract or Grant No.

69A355174110

12. Sponsoring Organization Name and Address

United States Department of Transportation
Research and Innovative Technology Administration
1200 New Jersey Avenue, SE
Washington, DC 20590

13. Type of Report and Period Covered

Final Report

14. Sponsoring Agency Code

15. Supplementary Notes

Report uploaded to: www.pactrans.org

16. Abstract

The metric derived from the longitudinal profile IRI (international Roughness Index) is a substantial input for the majority transportation agencies' highway monitoring systems used to improve road safety, increase road quality, and reduce fuel consumption. Traditionally, authorities have used data collected by inertial profilers to evaluate IRI; however, these instruments are usually unfeasible for data collection in smaller areas, and their narrow field-of-view (FOV) produces inadequate context for the scene. Meanwhile, uncrewed aircraft systems (UAS) have been widely used in a variety of transportation applications because of their efficiency and affordability in acquiring high-quality data. Especially for smaller areas, through the Structure from Motion (SfM) technique, UASs are a promising complementary tool for conducting ground surveys because they can provide good 3D context with high-resolution images. However, the SfM approach has some limitations for predicting the accuracy and quality of produced point clouds because of some factors such as surface texture, lighting conditions, processing algorithms/software etc. Our study aimed to assess the feasibility and data accuracy of the SfM technique for evaluating IRI by considering its limitations. This study also sought to build a framework for obtaining IRI metrics from an SfM-derived point cloud and to provide recommendations for collecting and processing UAS data with the goal of extracting pavement information.

17. Key Words	18. Distribution Statement
Smoothness/Roughness Measurement, UAS, SfM, Terrestrial LIDAR, IRI, Point Cloud, DEM	

19. Security Classification (of this report)	20. Security Classification (of this page)	21. No. of Pages	22. Price
Unclassified.	Unclassified.	31	N/A

Form DOT F 1700.7 (8-72) **Reproduction of completed page authorized.**

SI* (MODERN METRIC) CONVERSION FACTORS

APPROXIMATE CONVERSIONS TO SI UNITS

Symbol	When You Know	Multiply By	To Find	Symbol
		LENGTH		
in	inches	25.4	millimeters	mm
ft	feet	0.305	meters	m
yd	yards	0.914	meters	m
mi	miles	1.61	kilometers	km
		AREA		
in^2	square inches	645.2	square millimeters	mm^2
ft^2	square feet	0.093	square meters	m^2
yd^2	square yard	0.836	square meters	m^2
ac	acres	0.405	hectares	ha
mi^2	square miles	2.59	square kilometers	km^2
		VOLUME		
fl oz	fluid ounces	29.57	milliliters	mL
gal	gallons	3.785	liters	L
ft^3	cubic feet	0.028	cubic meters	m^3
yd^3	cubic yards	0.765	cubic meters	m^3
	NOTE: volumes greater than 1000 L shall be shown in m^3			
		MASS		
oz	ounces	28.35	grams	g
lb	pounds	0.454	kilograms	kg
T	short tons (2000 lb)	0.907	megagrams (or "metric ton")	Mg (or "t")
		TEMPERATURE (exact degrees)		
°F	Fahrenheit	5 (F-32)/9 or (F-32)/1.8	Celsius	°C
		ILLUMINATION		
fc	foot-candles	10.76	lux	lx
fl	foot-Lamberts	3.426	$candela/m^2$	cd/m^2
		FORCE and PRESSURE or STRESS		
lbf	poundforce	4.45	newtons	N
lbf/in^2	poundforce per square inch	6.89	kilopascals	kPa

APPROXIMATE CONVERSIONS FROM SI UNITS

Symbol	When You Know	Multiply By	To Find	Symbol
		LENGTH		
mm	millimeters	0.039	inches	in
m	meters	3.28	feet	ft
m	meters	1.09	yards	yd
km	kilometers	0.621	miles	mi
		AREA		
mm^2	square millimeters	0.0016	square inches	in^2
m^2	square meters	10.764	square feet	ft^2
m^2	square meters	1.195	square yards	yd^2
ha	hectares	2.47	acres	ac
km^2	square kilometers	0.386	square miles	mi^2
		VOLUME		
mL	milliliters	0.034	fluid ounces	fl oz
L	liters	0.264	gallons	gal
m^3	cubic meters	35.314	cubic feet	ft^3
m^3	cubic meters	1.307	cubic yards	yd^3
		MASS		
g	grams	0.035	ounces	oz
kg	kilograms	2.202	pounds	lb
Mg (or "t")	megagrams (or "metric ton")	1.103	short tons (2000 lb)	T
		TEMPERATURE (exact degrees)		
°C	Celsius	1.8C+32	Fahrenheit	°F
		ILLUMINATION		
lx	lux	0.0929	foot-candles	fc
cd/m^2	$candela/m^2$	0.2919	foot-Lamberts	fl
		FORCE and PRESSURE or STRESS		
N	newtons	0.225	poundforce	lbf
kPa	kilopascals	0.145	poundforce per square inch	lbf/in^2

*SI is the symbol for the International System of Units. Appropriate rounding should be made to comply with Section 4 of ASTM E380.
(Revised March 2003)

TABLE OF CONTENTS

LIST OF FIGURES

LIST OF TABLES

LIST OF ABBREVIATIONS

ALS:	Airborne laser scanning
AOI:	Area of interest
BBI:	Boeing Bump Index
DEM:	Digital elevation model
DMI:	Distance measuring instrument
DOT:	Department of Transportation
FAA:	Federal Aviation Administration
FOV:	Field-of-view
GCP:	Ground control points
GNSS:	Global navigation satellite system
GSD:	Ground sampling distance
HRI:	Half-car Roughness Index
IMU:	Inertial measurement unit
IRI:	International Roughness Index
LiDAR:	Light detection and ranging
MLS:	Mobile laser scanning
MRI:	Mean Roughness Index
MVS:	Multi-view stereo
ODOT:	Oregon Department of Transportation
PacTrans:	Pacific Northwest Transportation Consortium
PCC:	Portland cement concrete
PMS:	Pavement Management System
PPK:	Post-Processed Kinematic
RMSD:	Root-mean-square deviation
RTK:	Real-time kinematic
SfM:	Structure from Motion
TLS:	Terrestrial laser scanning
UAS:	Uncrewed (unmanned) aircraft systems
WSDOT:	Washington State Department of Transportation

ACKNOWLEDGMENTS

The research team would like to recognize and express sincere appreciation to PacTrans (Regional University Transportation Center for Region 10) for its financial support of this project and to the Oregon Department of Transportation (ODOT) for providing the data. The authors also thank Andrew Senogles for his participation in the data collection and processing. The team would like to acknowledge Lecia Geosystems and David Evans and Associates for providing equipment and software. The software Cloud Compare and ProVAL were also used in this study.

EXECUTIVE SUMMARY

The metric derived from the longitudinal profile IRI (international Roughness Index) is a substantial input for the majority transportation agencies' highway monitoring systems used to improve road safety, increase road quality, and reduce fuel consumption. Traditionally, authorities have used data collected by inertial profilers to evaluate IRI; however, these instruments are usually unfeasible for data collection in smaller areas, and their narrow field-of-view (FOV) produces inadequate context for the scene. Meanwhile, uncrewed aircraft systems (UAS) have been widely used in a variety of transportation applications because of their efficiency and affordability in acquiring high-quality data. Especially for smaller areas, through the Structure from Motion (SfM) technique, UASs are a promising complementary tool for conducting ground surveys because they can provide good 3D context with high-resolution images. However, the SfM approach has some limitations for predicting the accuracy and quality of produced point clouds because of some factors such as surface texture, lighting conditions, processing algorithms/software etc. Our study aimed to assess the feasibility and data accuracy of the SfM technique for evaluating IRI by considering its limitations. This study also sought to build a framework for obtaining IRI metrics from an SfM-derived point cloud and to provide recommendations for collecting and processing UAS data with the goal of extracting pavement information.

KEYWORDS: Smoothness/Roughness Measurement, UAS, SfM, Terrestrial LiDAR, IRI, Point Cloud, DEM

CHAPTER 1. INTRODUCTION

1.1. Background

To ensure travelers' comfort, safety, and fuel efficiency, roadways must be in decent condition and functional (Louhghalam et al., 2015). To achieve such goal, transportation agencies heavily rely on an automated Pavement Management System (PMS) to monitor and assess road conditions. Information from the PMS aids decision-makers in making consistent, cost-effective decisions through good management practices to keep pavements in serviceable condition (Ragnoli et al., 2018). Roughness statistics, along with surface distress, skid resistance, rutting, and structural capacity, are among the most critical factors for pavement management systems when pavement data are analyzed. Surface roughness in general refers to the degree to which a road's surface deviates from a perfectly flat plane along axes such as longitudinal profile, transverse profile, and cross slope. Deteriorated pavements are usually associated with higher surface roughness (Fakhri et al., 2021), while smooth roads have numerous advantages, such as requiring less maintenance, being safer for vehicles, experiencing less dynamic stress than roads with a rough surface, lasting longer, and being more solid (De Blasiis et al., 2020; ASTM E1926-08, 2021; Olsen et al., 2012).

1.1.1. Road Roughness Indices

Numerous roughness dynamic indices are used to determine the roughness/smoothness of the pavement. The most common ones are the International Roughness Index (IRI), the Profilograph Index (PrI), the Quarter-car Index, the root-mean-square vertical acceleration, and the rod and level surface smoothness measurement (Zak, 2016). IRI was founded in 1982 through a joint effort involving institutions from around the globe, road maintenance departments and agencies, research institutes, and the World Bank in order to standardize the measurement of roughness across organizations and eliminate inconsistencies that had previously resulted from the use of different instruments and approaches (Sayers, 1986). It became the most extensively used roughness index (Cruz et al., 2021; Karamihas, 2021; Múčka, 2017; Olsen et al., 2012) because of its reproducibility and stability over time (Sayers, 1998). Currently, the majority of U.S. state departments of transportation (DOTs) use the IRI to evaluate pavement roughness (Ong et al., 2010; Smith et al., 2016). The World Bank has taken entire control of the definition of standards and recommendations for this index (Thomas, 2021).

The ASTM E1926-08 standard defines IRI as a mathematical processing of longitudinal profile data to provide road roughness statistics that correspond to cumulative units of slope suspension motions divided by the distance traveled with a quarter-car model at 80 km/h (50 mph) (Cruz et al., 2021; ASTM E1926-08, 2021; Olsen et al., 2012). This quarter-car model (also known as the Golden Car) models the impact of a single tire system on the road surface. It comprises one wheel represented by a vertical spring, axle mass supported by the tire, a suspension spring and damper, and vehicle body mass supported by the suspension (Sayers, 1989). As a result, it is typically stated as a ratio, such as meters per kilometer or inches per mile (figure 1.1).

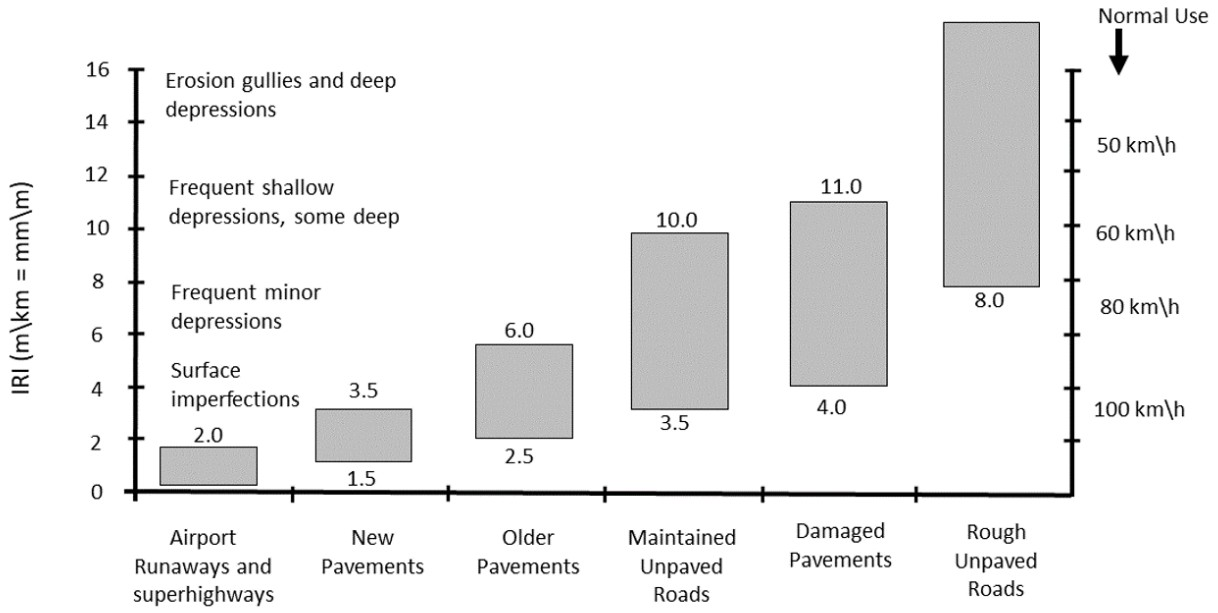

Figure 1.1. The IRI roughness scale (Elghriany et al., 2016; Sayers, 1986)

Some important considerations for determining the IRI value are listed as follows based on previous studies (Olsen et al., 2012):

- The IRI calculation relies on the longitudinal profile qualities being measured accurately. Hence the elevation profile measuring equipment utilized with this technique must be up to the task.
- The precision of the IRI is dependent on the interval between consecutive profile elevation measurements; hence, decreasing the spacing often improves precision. A

maximum interval of 0.3 m (12 in.) is recommended by ASTM standards (ASTM E1926-08, 2021)

- To simulate the tire encircling effect of tires, the moving average filter uses a low pass filter of 9.85 in (250 mm) to smooth the profile by using the average values of adjacent points.
- Localized roughness is shown separately because rough areas will be averaged out when a long length is used to provide IRI. Localized roughness is defined as any 25-foot (7.62-meter) segment with IRI values, which has a disproportionate effect on the overall IRI.

1.1.2. Road Profile Measurement

Road surface profiles, which illustrate the elevation variations of a road over a certain distance, can be measured by using a variety of devices for both new and existing pavements (Olsen et al., 2012). The ASTM E 950-94 standard groups roughness measuring equipment into four classes based on survey accuracy (Bennett et al.,2006; Olsen et al., 2012; Prosser-Contreras et al., 2020; Radović et al., 2016; Thomas, 2021):

- **Class 1 -** indicates the highest accuracy and, regardless of speed, corresponds to a longitudinal profile with a vertical precision of 0.5 mm (non-contact lightweight profiling devices, portable laser profilers, dipsticks).
- **Class 2 -** takes into account alternative profiling strategies for IRI measurement in which a longitudinal profile is required (Profilographs, optical and inertial profilers).
- **Class 3 -** incorporates measurements of correlation, which imply a mathematical calculation is needed to acquire the result, and so represents a lower quality level (Roadmaster, ROMDAS).
- **Class 4 -** reflects the use of subjective procedures and measurements that have not been calibrated (visual inspection, ride over section etc.).

Rod and level, inclinometer-based profilers (Walking Profilers etc.) and Profilographs are the conventional tools used for collecting data during roughness evaluations. Each of these conventional methods has some distinct advantages. Rod and level grade surveys combined with static profilometer surveys may produce an exceptionally precise (sub-millimeter) profile of the roadway, which is why they are frequently referred to as the "TRUE profile" (Olsen et al., 2012; Sayers, 1995). Manually controlled walking profilers, or inclinometer-based profilers, are

substantially faster than the rod and level technique while often providing a real-time display of the data. Profilographs can collect continuous profile data through a wheel-track (Smith et al., 2016).

However, these conventional methods can suffer from several drawbacks. First, all the aforementioned measuring instruments and techniques require lane closure or some traffic control. Additionally, only one wheel route can be measured at a time, and some systems are limited to the operation speed limit. As a result, it is especially challenging to utilize these systems and techniques for high-traffic routes or large areas, as they can be time-consuming and prone to safety hazards. Moreover, sufficient expertise and extensive training are required for implementation teams to be able to efficiently acquire high quality data. Fortunately, General Motors Laboratories invented inertial profilers as a groundbreaking advancement in pavement roughness measuring. Laser profilers are now the dominant asphalt pavement data collection instrument for most transportation agencies (Ong et al., 2010; Smith et al., 2016). These systems utilize an accelerometer to track the frame's (vehicle's) motion and noncontact laser sensors to track the frame's vertical movement relative to the road surface with a constant interval. Simultaneously, a distance measuring instrument (DMI) keeps track of the travel distance along the highway during data collection. The combination of these characteristics produces the longitudinal profile of the road.

Although inertial and laser profilers provide great accuracy, efficiency, and mobility, there are still a few significant constraints. First and foremost, during data collection, speed needs to be consistent, and it is not recommended to use a profiler at speeds lower than 15 kilometers per hour (Sayers, 1998). For example, it would be challenging to deploy high-speed profilers at highway speeds in heavy traffic or to sustain its high pace consistently (Lee et al., 2010), especially in urban areas (Loizos et al., 2008; Prosser-Contreras et al., 2020). Some studies have coped with this by modifying the quarter car model's parameters or by filtering the data based on certain criteria (De Blasiis et al., 2020). However, such methods may increase the workload and require more time for both data collection and processing. Another shortcoming of high-speed inertial profilers is the variation in the vehicle's trajectory. In other words, the profiles may not precisely align with the road alignment, and therefore a detailed comparison between elevation profiles, rather than the aggregated IRI values, is challenging for some applications, such as in tracking changes in the road surface (Lee et al., 2010). The other

drawback of profilers is their intrinsically limited field-of-vision (FOV), which makes it challenging to obtain a comprehensive understanding of the overall context of the scene, particularly on roadways that have been damaged. Furthermore, some profilometers struggle in measuring severely damaged or stone/dirt roads with high-frequency variations (De Blasiis et al., 2020). Lastly, inertial profilers are relatively more expensive to mobilize than emerging technologies such as ground- or UAS-based photogrammetric technologies for evaluating shorter sections.

1.1.3. Remote Sensing Technologies

The advent of state-of-the-art remote sensing technology has opened up a substantial window of opportunities for transportation agencies by addressing some of the aforementioned shortcomings of profilers (De Blasiis et al., 2020). In contrast to earlier profiling technologies, remote sensing technology can be a much more economical solution (it has been widely used for applications such as topographic mapping), and the data can be re-used for measuring elevations along a profile (Olsen, 2013; Olsen et al., 2012).

Light detection and ranging (LiDAR) is one of the most promising approaches among the remote sensing technologies for use in the built environment at the present time (Barbarella et al., 2017; De Blasiis et al., 2020; Schnebele et al., 2015) because of its high efficiency and accuracy (White et al., 2010) (Olsen et al., 2009). Based on a platform equipped with a lidar sensor, lidar systems can be usually categorized into airborne laser scanning systems (ALS), mobile laser scanning systems (MLS), and terrestrial laser scanning systems (TLS). ALS is able to capture a very large area efficiently and is widely used for topographic mapping (Shan et al., 2018; Vosselman et al., 2010). However, the point density is usually not sufficient for capturing geometric details on the road surface because of the longer distance between the system and the objects. It is also not feasible for more frequent monitoring, given its cost and logistics. MLS and TLS are more suitable for capturing the road surface and assessing road characteristics. Additionally, more and more automated approaches have been developed for a variety of feature extraction tasks to help improve the workability of the laser scanning data (Che et al., 2019). MLS and TLS have proved to be sufficiently accurate and efficient for quantifying surface roughness (e.g., IRI) in comparison to to conventional rod-and-level surveys and inertial profiler systems (Olsen and Chin, 2012; De Blasiis et al., 2020).

In recent years, unmanned aircraft systems (UAS) have become a preferred alternative to the aforementioned technologies for many civil infrastructure applications (Dobson et al., 2013), including road pavement condition assessment evaluations (Nappo et al., 2021). This is because of their significant impact on cutting costs while boosting safety, efficiency, resolution, and accuracy through the use of constantly expanding hardware and software technologies that help them to reconstruct 3D models from two-dimensional images (e.g. Agisoft Metashape, Pix4D mapper, Visual SfM) (Greenwood et al., 2019; Voumard et al.,2018).

In comparison to ALS, UASs are able to survey at a much lower altitude to capture greater details on the road surface with a bird's-eye perspective of the region of interest (Fonstad et al., 2013). On the other hand, drone pilots can stay away from the road and traffic, resulting in a safer operation than ground-based LiDAR systems. Moreover, UASs are much more cost effective and easier to access while requiring fewer logistics than ALS, MLS, and TLS surveys. In addition, given Federal Aviation Administration (FAA) flight duration and other restrictions (e.g., visual contact requirements with the UAS during flight), UASs are more suitable for gathering data for less than 2 square kilometers (Simpson, 2018).

The revolutionary photogrammetry techniques that include Structure-from-Motion (SfM) and multi-view stereo (MVS) have been widely applied thanks to the rapid development of computer vision algorithms. They enable 3D models to be constructed from 2D images by utilizing image processing that applies a collection of algorithms to locate and identify points captured by UASs in a series of photos (Prosser-Contreras et al., 2020) without having knowledge of the camera's location and orientation or reference points in the scene. They also enable users to automatically resolve or refine calibration issues during the process (Iglhaut et al., 2019). All of these significantly reduce the number of ground control points (GCP) required for a successful 3D reconstruction. In principle, with global navigation satellite system (GNSS) measurements—sometimes with the aid of inertial measurement units (IMU)—collected during a flight that record the position and orientation of each camera frame, a decent 3D model can be generated without any ground control point. This can be very beneficial for areas that are difficult to access. That being said, to ensure the quality of the 3D models, evenly distributed and accurately surveyed ground control points across the area of interest are highly recommended (Fonstad et al., 2013). The data products from this process can include various types and formats,

including 3D point cloud, digital elevation model (DEM), orthomosaic image, triangular mesh, and so on.

1.2. Literature Review

As one of today's cutting-edge technologies, UASs have proved to be a useful tool for conducting accurate surveys (Varbla et al. 2021) and have rapidly gained popularity in civil engineering applications. One application is to evaluate pavement distress by leveraging IRI with UAS-SfM-produced point clouds. This section presents a review and overview of various studies that have used 3D point clouds and related techniques for pavement assessment.

The most common pavement evaluation methods (e.g., inertial and walking profiler, etc.) are effective and efficient. However, they can be costly, especially for a relatively small area of interest, disruptive to traffic, and unable to provide a large context for the scene (Greenwood et al., 2019). To utilize UAS-SfM as an alternative, since it can produce high quality 3D point clouds, Inzerillo et al.(2018) demonstrated the validity of UAS image-derived 3D models for road condition surveys and for analyzing pavement distress deformations. Tan et al. (2019) and Saad et al. (2019) utilized oblique images acquired by UASs flying over an asphalt road at about 20 meters to detect and measure potholes with centimeter accuracy. More recently, Nappo et al. (2021) used 3D models reconstructed with UAS-SfM to evaluate the cracks on asphalt-paved roads subjected to landslides in Como, Italy. The researchers were able to quantitatively detect and describe longitudinal and transverse cracks wider than 1 cm, and the International Roughness Index (IRI) was computed to classify their severity. Nonetheless, a number of considerations need to be taken into account when pavements are evaluated using UAS-SfM, including accuracy, ground control points, flight altitude, surface characteristics, and so on (Javadnejad et al., 2021).

Accuracy of the data products (e.g., point clouds, DEM, etc.) plays an important role in the 3D representation of the pavement, especially for IRI calculations. One way to ensure the accuracy of the 3D reconstruction result is to set up ground control points (GCP). Liao et al. (2020) investigated how the number and distribution of GCPs can impact IRI values. However, the UAS platform in their study was not equipped with a GNSS receiver that was capable of real-time kinematic (RTK) positioning, which could have significantly improved data quality and efficiency without adding extra GCPs (Prosser-Contreras et al., 2020). Similarly, Agüera-Vega et al. (2017) presented their study on the impact of the number of GCPs in georeferencing on the

accuracy of the DEM and orthomosaic image. This research revealed that increasing the number of GCPs improved horizontal and vertical accuracy. The experiment showed that more GCPs would reduce the uncertainty of the 3D reconstruction process. In addition to the GCPs, Varbla et al. (2021) included flight altitude in their analysis of UAS-SfM data for detecting road structure deformation. The study concluded that the ideal number of required GCPs decreased as survey altitude increased, which means that georeferencing accuracy started declining when the recommended number of GCPs was surpassed.

Although in principle a lower flight altitude can result in higher accuracy and resolution of the 3D point cloud (Saad et al., 2019; Tan et al., 2019; and Romero-Chambi et al., 2020), a UAS flight that is too low can disrupt or distract traffic, causing safety hazards (Hurwitz et al., 2018). As a result, despite the fact that some studies have demonstrated that a very low altitude (e.g., 10 m) can yield a 3D point cloud with very high resolution and accuracy (Prosser-Contreras et al., 2020), such flight parameters are not applicable for highways that have more severely damaged pavement and high-volume traffic. For this reason, Zeybek et al. (2021) examined the impact of flying height on the accuracy of resulting 3D point clouds for IRI evaluations. The study tested flying heights of 35 m and 50 m and found no significant difference in point cloud resolution and IRI evaluation results.

Because the SfM process relies on the contrast and features on the pavement surface captured in the images, the type of the pavement is an important consideration as well. Alhasan et al. (2015) compared the accuracy of point clouds acquired with TLS and terrestrial-based SfM for assessing road roughness over different types of surfaces, including gravel roads, Portland cement concrete (PCC), and one newly paved asphalt surface. Because of the low contrast and poor reflectivity of the fresh asphalt, insufficient points were captured for IRI computations in both the SfM and TLS data. Ward et al. (2019) also did a study using UAS-SfM and LiDAR to analyze airport pavement roughness based on Boeing Bump Index (BBI) and IRI values. On four distinct surface types—sand-asphalt, dirt, main runway asphalt, and a concrete pad—they compared results derived from UAS-SfM with the LiDAR data to assess accuracy. For the sand-asphalt surface and the concrete pad surface, the correlation between the LiDAR and UAS-SfM data utilizing both BBI and IRI parameters was found to be poor; however, the correlation was high for the brownish-colored dirt-strip surface. For the runway asphalt surface, the correlation between LiDAR and UAS-SfM data was low when the BBI parameter was used but acceptable

for the IRI parameter. Furthermore, the illumination conditions on the airfield were more ideal than those on a typical roadway, since there were limited vertical obstructions near the airport to cause shadows.

Moreover, even under the same conditions, the algorithms and implementations in the SfM software can be different while the parameter settings have a significant impact on the accuracy of the resulting point clouds (Slocum et al., 2017). Agisoft Metashape and Pix4D Mapper are two of the most well-known commercial SfM-based programs. Zeybek et al. (2021) compared them and concluded that Agisoft Metashape is slightly better in terms of its accuracy and efficiency, but only in their specific test settings. However, it is challenging to establish a well-controlled experimental setting, especially given the variable outdoor environment. Fortunately, Slocum et al. (2017) proposed a workflow, named simUAS, that generates virtual UAS surveys in a simulated graphical environment that can be used to test a wide variety of factors (e.g., lighting, texture, topography, flight altitude, camera resolution, etc.).

1.3. Objectives of This Study

As discussed in the previous sections, UAS-SfM can be a great tool for assessing and monitoring a relatively small area, especially for those that are subject to geohazards (e.g., landslides) and need frequent maintenance and repair. Such areas usually feature multiple types of pavements and more variation in surface roughness, resulting in various errors and artifacts (figure 1.2), while most of the existing work has focused on road sections with uniform pavement. Therefore, in this project, the research team developed a framework for obtaining pavement roughness metrics (e.g., IRI) from UAS-SfM and validated the feasibility of using UAS-SfM point clouds to assess pavement. A rigorous accuracy analysis was conducted to evaluate the accuracy of the UAS-SfM point clouds, the DEM, and the IRI value by comparing them with TLS scans and control survey results. Furthermore, the research team provided recommendations and considerations about utilizing UAS-SfM in road roughness assessment by including both field practice and procedures in the workflow.

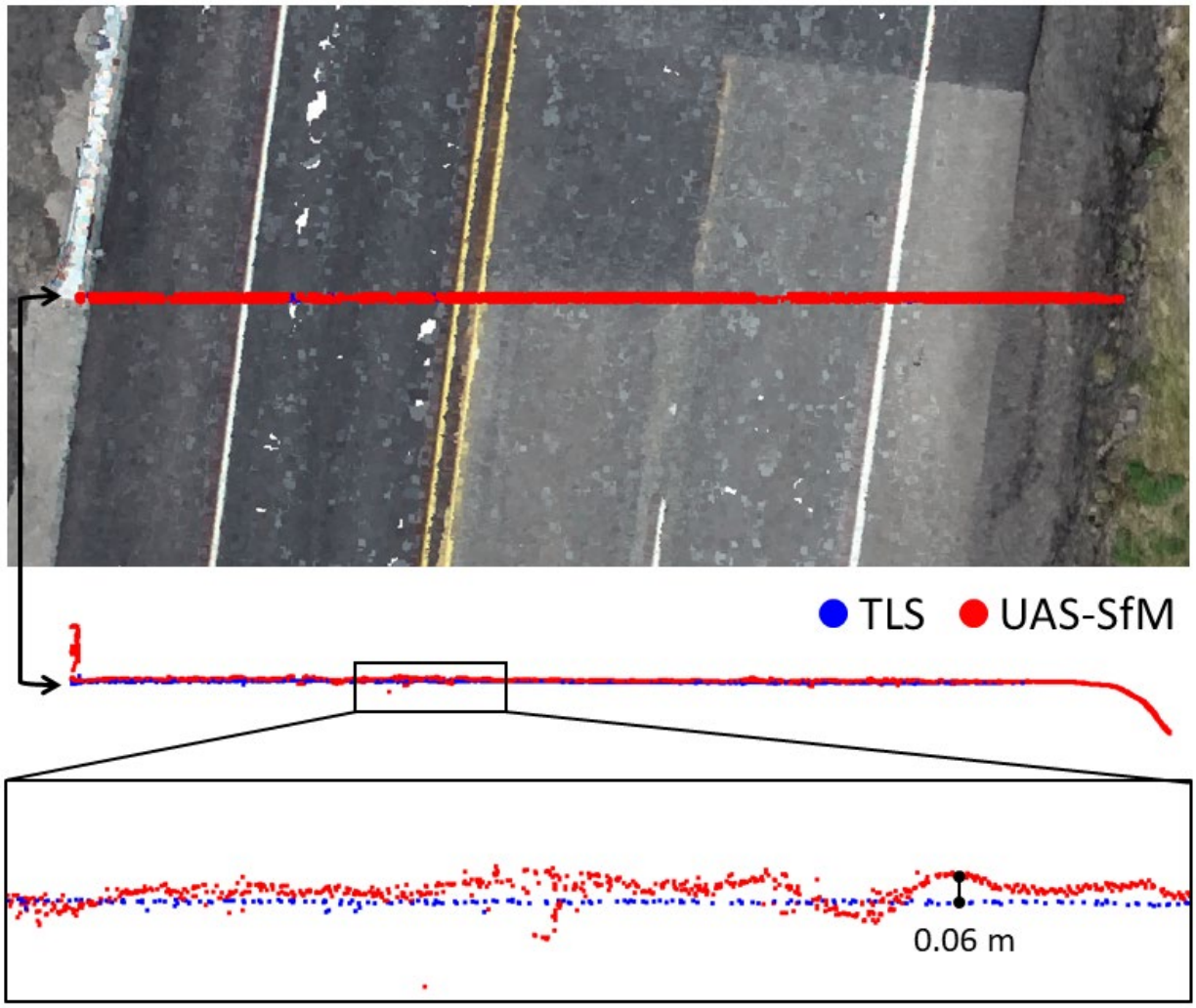

Figure 1.2. Example of a road profile of TLS and UAS-SfM point clouds.

CHAPTER 2. MATERIALS AND METHODS

2.1. Overview

The project was conducted at a site called Arizona Inn along the Oregon Coast Highway (U.S. Route 101) (figure 2.1) on June 14, 2021. An active landslide at the site was causing damage to the road surface. As a result, the pavement needed to be repaired very frequently. The proposed effort aimed to demonstrate the possibility of employing UAS-based point cloud data to estimate pavement roughness. To achieve this objective, the research team acquired aerial photos with a UAS and generated point clouds utilizing the Structure from Motion (SfM) processing technique. The point clouds were then converted into a digital terrain model (DEM), which was then used to calculate the roughness/smoothness metrics (i.e., IRI) of the road surface. In addition, total station measurements on the road surface and terrestrial LiDAR scans were collected for comparison and analysis. The equipment used in the field effort is listed in table 2.1.

Table 2.1. Key equipment list for the field effort

INSTRUMENT LIST
Riegl VZ400 Laser Scanner with Nikon D700 Digital Camera
Leica GS14 GNSS Receiver
DJI Phantom 4 Pro RTK UAS
Leica TS15P 1” Total Station
Leica 360° prism with bipod
2’ x 2’ Iron Cross Targets

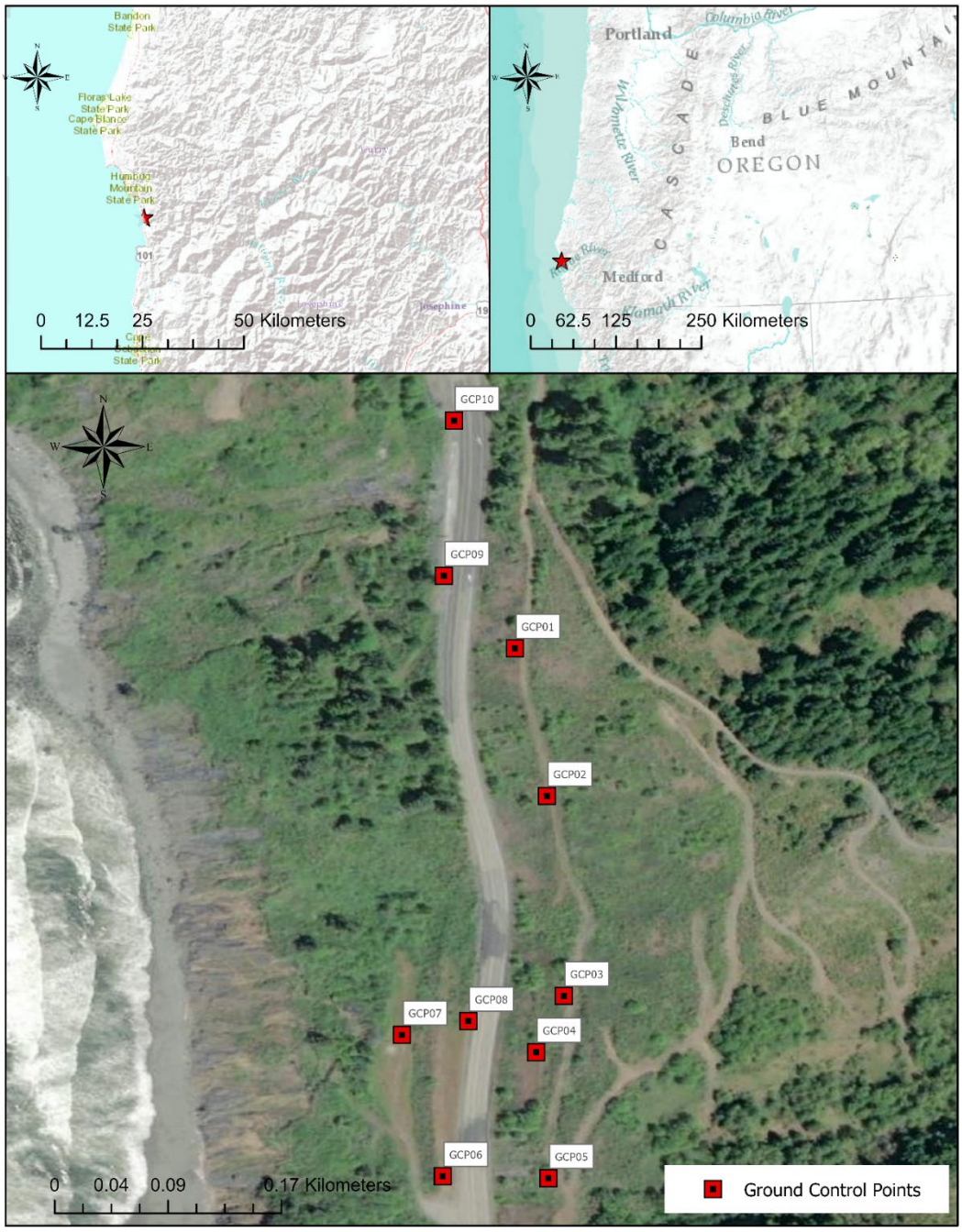

Figure 2.1. Satellite imagery and site map of the study area with ground control points marked.

2.2. GNSS and Total Station Survey

GNSS was used to determine the positions of ten ground control points (GCPs) across the site (figure 2.1) and each terrestrial LiDAR scan station. The locations of the GCPs were planned and set up based on the following considerations: even distribution throughout the proposed area;

personnel safety (i.e., not located near abrupt cliffs or near traffic); and sky visibility for both GNSS and UAS imagery data collection. For all the GNSS surveys, a minimum of 5-minute observations were taken at a 1-Hz data rate. The coordinates of this base station were computed by utilizing OPUS-Projects v4.12, which referenced the base station to six of the nearest National Geodetic Survey (NGS) Continuously Operating Reference Stations (CORS) located approximately 80 km, on average, from the project site. Leica Infinity v3.4 was then used to compute baseline vectors in relation to a local GNSS base station set up on the project site by using the Post-Processed Kinematic (PPK) approach.

Additionally, a total station survey was performed with a Leica TS15P 1-in. instrument to provide more check points to validate the terrestrial LiDAR and UAS-SfM data. The GCPs were captured with a Leica 360° prism, while all the check points on the road surface were acquired with reflectorless observations because of safety concerns. A total of 180 checkpoints were observed in seven different profiles, including four profiles parallel to the flow of traffic and three profiles perpendicular to the flow of traffic (figure 2.2).

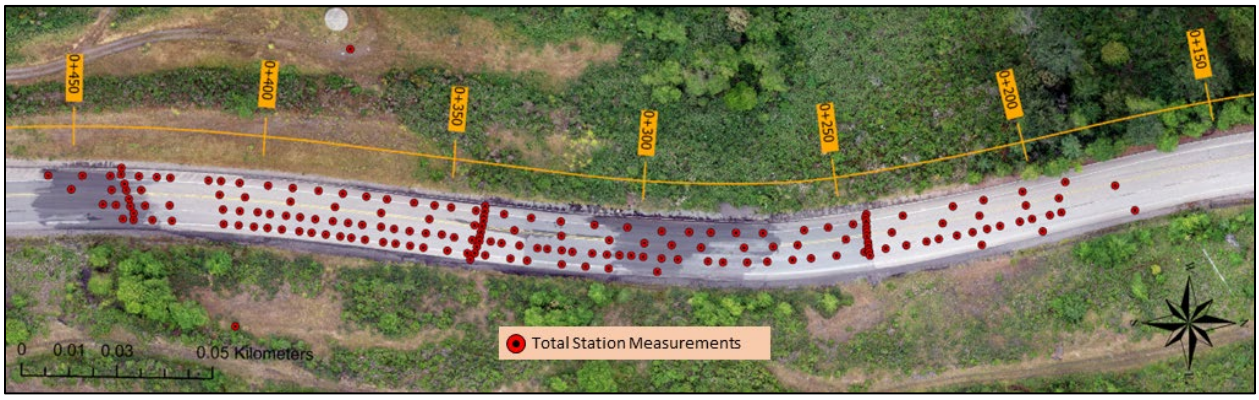

Figure 2.2. The check points on the road surface surveyed by the total station.

All resulting data from the GNSS and total station surveys were combined via a least square adjustment performed in MicroSurvey Star*NET v10.0. The resulting coordinates were projected in OCRS Oregon Coast, in which the horizontal datum was North American Datum of 1983 (2011) epoch 2010.00. Geoid12B was used to obtain the orthometric height of the data points, which were referenced to the North American Vertical Datum of 1988 (NAVD88).

2.3. Terrestrial LiDAR Data

A total of 17 terrestrial lidar scans with images were collected with a Riegl VZ-400 to cover the entirety of the area of interest (figure 2.3). The scanner was set up on both sides of the road to increase the overall point density as well as to mitigate the occlusions caused by moving vehicles. The typical scan resolution was around 0.05° horizontally and vertically, which could result in an approximate point spacing of 1 cm at 10 m away from the scan set-up. Note that the point spacing increased with an increasing range from the scanner. Therefore, it was important for the scan positions to not be spaced closely together such that a more homogenous point density could be achieved throughout the project area. With the GNSS receiver mounted on top of the scanner, the global coordinates of each scan could be acquired and processed in relation to the base station, similarly to processing of the GCPs, which could substantially simplify the initial alignment of the scans. The registration of the initial aligned scans was further refined by using the PointReg software utilizing a cloud-to-cloud matching algorithm known as ICP (Iterative Closest Point). This workflow balanced between absolute geo-referencing accuracy and relative local accuracy via GNSS measurements and cloud-to-cloud matching, respectively.

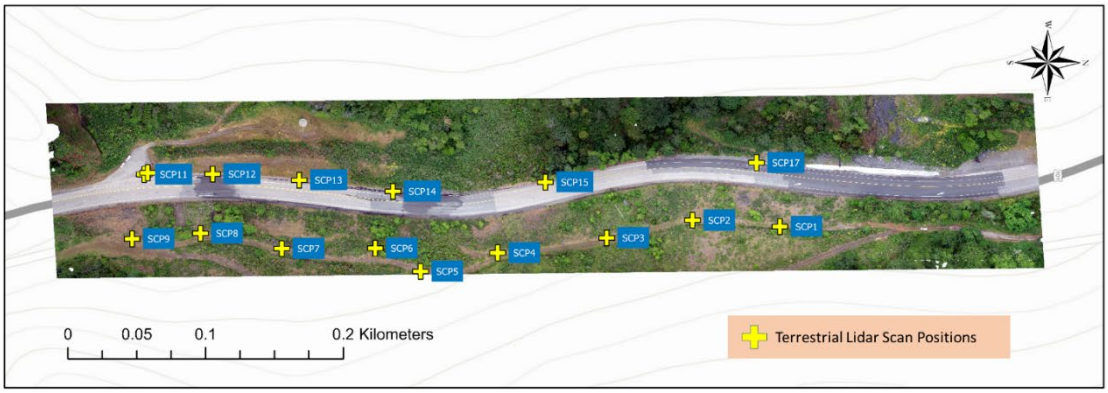

Figure 2.3. Terrestrial LiDAR scan positions within the project area.

2.4. UAS-SfM Data

A DJI Phantom 4 RTK drone was deployed to capture red, green, blue (RGB) imagery for 3D reconstruction based on the SfM technique in this study. Special care was taken in setting

the image acquisition parameters for the camera, including ISO range, shutter speed, aperture, and white balance (table 2.2). All imagery was captured and processed in the .jpeg file format. The raw file format is generally preferred, as it maintains all data acquired by the sensor while providing a high dynamic range that can decrease the total area of poorly exposed features in an image. Unfortunately, not all the software/firmware supported the collection or processing of raw files. The image acquisition settings were chosen on the basis of a previous survey of the site for topographic mapping and change detection. Specifically, the controlling parameters were the ground sampling distance (GSD), which was set to be 1.4 cm per pixel (~48.8 meters above ground level), and overlap/sidelap percentages, which were both set to be 80 percent. Note that the UAS survey was not performed directly over the roadway with a low flight altitude to minimize the distraction to drivers.

Table 2.2 UAS and camera specifications

Make/Model:	**DJI P4 RTK**
Resolution (pix):	**5472 x 3648**
Pixel Size (µm):	**2.41 x 2.41**
Focal Length	**8.8**
File Format:	**.jpeg**
Shutter Speed	**Auto [1/100,**
Aperture:	**f/4**
ISO:	**Auto [100, 400]**
Focus:	**Auto (center)**

The trajectory of the UAS was derived via GNSS relative positioning between the UAS and the GNSS base stations discussed in section 2.2. The open-source GNSS processing software package RTKLIB (Takasu and Yasuda, 2009) was used in post processing kinematic (PPK) positioning mode to compute the remote aircraft's trajectory. Using a custom Python script, the camera positions and their covariances were extracted from the GNSS trajectory, transformed to the desired map projection, and used as input in Agisoft Metashape for SfM processing. Note that using the PPK GNSS positions of the acquired images reduced the need for ground control points when SfM software was used, thereby decreasing the total data acquisition time. The position (X, Y, Z) of each photo was attained from the PPK trajectory and were used to seed the SfM algorithm. These seeded image coordinate values aided the SfM algorithm by constraining the position for each photo, rather than having he algorithm rely on established ground control points. This allowed the algorithm to better refine the position (X, Y, Z) through

the use of a least squares bundle block adjustment while also determining the remaining extrinsic (roll, pitch, yaw) and intrinsic parameters of the camera. That being said, the GCPs were still used to provide the SfM software with more information to better compute the position and orientation of each image, as well as the intrinsic camera parameters. The resulting 3D point cloud from the SfM reconstruction is shown in figure 2.4.

Figure 2.4. UAS-SfM dense point cloud data representation of the highway

2.5. Point Cloud Processing

The point clouds from the UAS-SfM and terrestrial laser scanning (TLS) both included a lot of data off the road that were not relevant to this study. As a result, the point cloud data were cropped in CloudCompare, a commonly used, open-source 3D point cloud (and triangular mesh) editing and processing software.

Digital elevation models (DEMs) should be as error-free as feasible to provide a clear and accurate representation of the terrain or surface. For instance, the raw point clouds included non-ground objects such as cars as an isolated cluster in our dataset. Therefore, before creating a digital elevation model, the ground and non-ground points must be separated. This process, referred to as ground filtering, can be arduous and time consuming if done manually because of the amount of manual effort required. In this study, an effective and scalable versatile ground

filter based on multi-scale voxelization and smooth segments, named Vo-SmoG (Che et al., 2021), was used to accomplish the ground filtering.

It is also necessary to eliminate data gaps that develop as a result of various impediments that block the line of sight to the object of interest. These holes also may stem from portions captured with oblique scans when UASs scan near cliffs, especially for highway projects (Olsen et al., 2009). One way to diminish these holes is to increase the number of scans. In this project, fortunately, there were enough long- and short-range scans for the TLS data acquisition to minimize gaps/holes in the dataset (figure 2.3). Similarly, the high overlap and sidelap percentages (80 percent) of the UAS mission plan helped ensure that the project area was imaged thoroughly enough that the resulting UAS-SfM data had the least number of gaps and holes.

For some areas with data gaps, the alternative method is to fill these holes by predicting the topography in those areas with existing measurements. RAMBO software was used in this project to generate a DEM from point clouds and fill in the data gaps by using an iterative technique utilizing a thin plate spline. This method provided a smooth interpolation between a set of known points. However, note that the volume of holes is a criterion to decide whether hole filling is needed to accurately represent the surface. Thus, optimal results in estimating magnitude–frequency relationships and volumetric quantities occur when a proper balance between high modeling resolution and hole filling is struck (Olsen et al., 2015).This balance is adjusted by applying the hole filling parameters. After ground filtering and hole filling were completed, the terrain model was created with 0.1-m resolution with the RAMBO software.

2.6. IRI Computations

2.6.1. Profile Extraction

The pavement profiles for roughness calculation were created by using ArcGIS Pro version 2.9.0 software. The ArcGIS workflow is shown step-by-step in figure 2.5. Note that this workflow (except for the first step) was also implemented in Python by leveraging Arcpy library to improve efficiency, especially for batch processing.

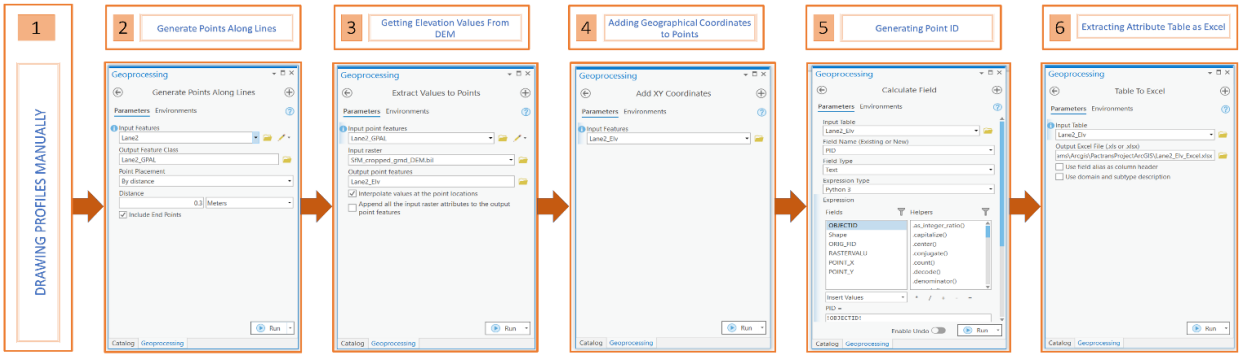

Figure 2.5. ArcGIS workflow

- Prospective pathways for the car wheels were manually created by using longitudinal road markings as guidelines, resulting in six longitudinal profiles, including four northbound and two southbound.
- The data point coordinates were extracted along these six profiles. Intervals of 0.3 m (12 in.) were used as recommended norms, according to standards (ASTM E1926-08, 2021).
- The points' elevations were computed by using the corresponding evaluation values in the DEM. The "*Interpolate Values at the point locations*" box was checked to use bilinear interpolation in case there was no data point in the DEM pixel.
- To produce consistency between point clouds and digital elevation models, the geographical coordinates (X and Y) were assigned to the points. A coordinate system also can be specified under the environment tab to produce consistency between data.
- The attribute table containing the point ID, geographical coordinates, and elevation information produced from the longitudinal profile was exported into a spreadsheet for the following analysis.

2.6.2. IRI Computations

IRI analyses were conducted by using ProVAL (Profile Viewing and Analysis) version 3.61.42. It is a software tool for viewing and analysis of longitudinal pavement profiles in a variety of ways (Transtec Group, 2016). Many pavement smoothness specifications, such as AASHTO, FHWA Federal Lands, and many US DOT specifications, cite it as the official standard analysis and reporting tool (Transtec Group, 2015).

The ProVAL software recognizes profile data both in text formats and in the two 4-byte floating-point binary formats. ERD is a file type adopted as a standard data format for analyzing and measuring road profiles. More information about the ERD files can be found in the paper by Sayers and Karamihas (1997). An ERD file is divided into two distinct sections: the header and the data. The header section contains basic information about the data (e.g., samples/channel, interval, storage format, unit, etc.) while the data section stores all the profile elevations (figure 2.6). In this study, the research team converted the output from the previous steps into an ERD file for each profile.

```
ERDFILEV2.00
    1, -1, -1, 1, 3, 0.3000000, -1,
TITLE   Track Run E1
SHORTNAMLElev.  LElev.
UNITSNAMft      m
XLABEL  Distance
XUNITS  m
END
```

Figure 2.6. Example ERD file header used in this study

Once the ERD files had been imported into ProVAL, the parameters shown in figure 2.7 were applied. For each profile in both the UAS-SfM and TLS data, the ProVAL's "Ride Quality" function was used, and a 250-mm filter was enabled for roughness computation. This function also provided three types of ride statistical analysis: *Overall*, *Continuous,* and *Fixed Interval*. The *Continuous* analysis type, which reported statistics for every sample location, was preferred for this project because it simulated a ride more realistically. Another criterion that had to be specified was the Ride Quality Index for which we would conduct the driving analysis. In addition to the IRI, which was the focus of this study, MRI (Mean Roughness Index) and HRI (Half-car Roughness Index) indices can also be analyzed with this function. Moreover, a segment length of 30 m was used, given the sampling interval (0.3 m) and the number of samples for each segment. There were two outputs of this process: a spreadsheet listing the maximum IRI values for each segment related to the location as distance, and a visual graph representation of the result.

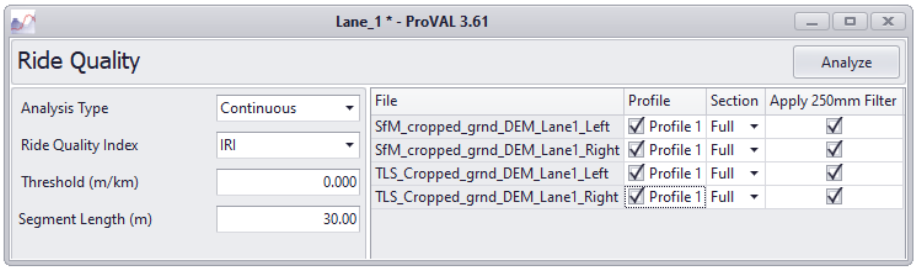

Figure 2.7. Applied ProVAL parameters

CHAPTER 3. ANALYSIS AND DISCUSSION

3.1. Vertical Accuracy Assessment

Before the UAS-SfM and TLS data were compared with each other, their vertical accuracy was first evaluated by comparing them with total station measurements. A total of 180 total station points were measured over the section between 200 m and 450 m of the study area. Most of these measurements were collected from the existing road lanes, while a few cross-sections were captured in the field. Because of safety considerations, all the measurements were made with reflector-less shots rather than prisms. The north side of the site (0 to 200 m along the highway) was not covered because of the limited field of view (figure 2.2).

The total station measurements were geo-referenced over the ground control points and compared with the DEM models derived from UAS-SfM and TLS data. A statistical analysis was then performed to further summarize the vertical accuracy (table 3.1). The vertical accuracy at the 95 percent confidence level was calculated as 1.96 $RMSE_Z$ (Eq 3.1), as stated in standards (Authority, 1998).

Table 3.1. Summary of vertical ccuracy (unit: meters)

	UAS-SfM	TLS
Average	0.017	0.035
Maximum	0.038	0.058
Minimum	-0.009	-0.007
Std. Deviation	0.008	0.014
RMSE	0.019	0.037
95% confidence	0.037	0.073

$$\boldsymbol{RMSEz} = \sqrt{\frac{\sum_{i=1}^{n}(Z_{data_i} - Z_{check_i})^2}{n}} \qquad \text{Eq. 3.1}$$

The statistical analysis showed that the vertical accuracy from both data sources was within a few centimeters. The standard deviations of the vertical errors were around 0.01 m, which in principle would support an IRI assessment, given that the bias (average error) would not affect the IRI assessment as significantly. Also note that despite the fact that the TLS data were intended to be used as control data, their overall vertical accuracy was lower than that of the UAS-SfM data. The following factors may have led to this situation:

- The UAS-SfM used the same ground control points as those used for georeferencing the total station data, which may have minimized vertical bias. Meanwhile, the TLS

was georeferenced with just GNSS post-processed kinematic (PPK) data collected from a receiver mounted on top of the scanner, independent from the GCPs except for the shared base station. As shown in the statistical analysis, the vertical accuracy of the TLS-derived DEM was in line with the typical accuracy of GNSS measurements.

- The smoothing process during the DEM generation was relatively more effective in filtering the noise in the UAS-SfM point cloud, partially because it typically had a more uniform point distribution than the TLS, which was heavily affected by range and angle of incidence.
- The total station measurements were mostly taken on or near the pavement markings, where the UAS-SfM showed superior performance because the high contrast provided more key points for matching and 3D reconstruction. One the other hand, although reflective markings could be captured in a longer range for the TLS, the TLS scans could suffer from an oblique angle and long range because the larger footprint of the laser beam could introduce more ranging errors.

3.2. DEM Overview

The digital elevation models generated from the UAS-SfM, and TLS point clouds were compared visually and quantitatively in this study. These analyses were conducted with a series of data products from both data sources, including an orthomosaic image, digital elevation models (enhanced via hillshade), and the difference between DEMs (figure 3.1). More closeup views to certain features are shown in the section focusing on localized analysis (section 3.3).

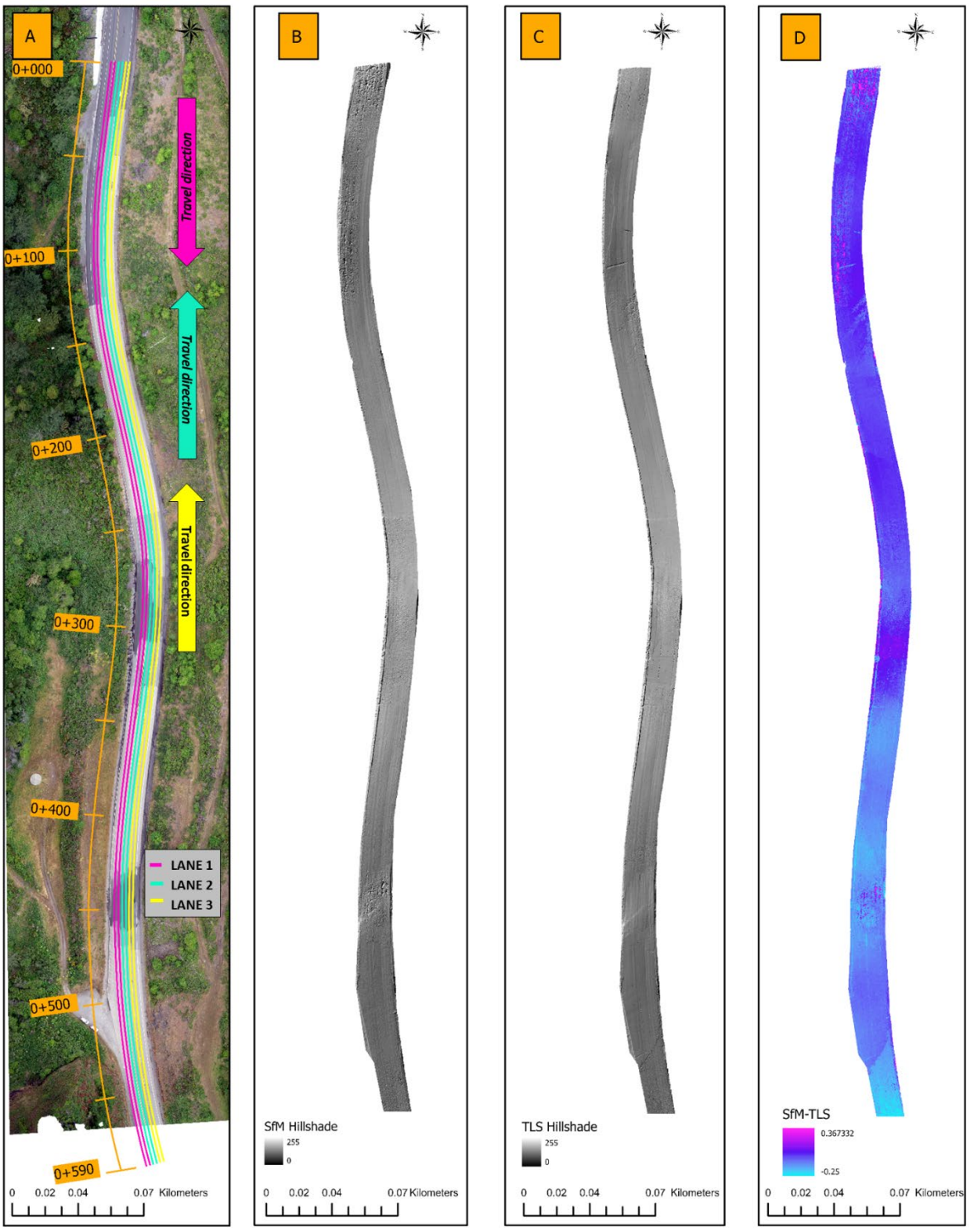

Figure 3.1. Overview of the data products from the TLS and UAS-SfM. A) An Orthomosaic of the pavement, B) UAS-SfM-derived DEM`s hillshade map, C) TLS-derived DEM`s hillshade map, D) The vertical difference UAS-SfM and DEM data representation.

The orthomosaic shows an overview of the area of interest (AOI), including three newly paved portions (figure 3.1 (A)). Note the AOI was referenced with the local mileage starting from north to south. Between 0 and 150 m of the AOI, the west side of the road (the lanes on the left in the map) had been newly paved with asphalt, resulting in a very dark surface. In the same area, significant rough artifacts occurred in the UAS-SfM DEM, corresponding to the darker area in figure 3.1 (B). On the other hand, this section appears substantially smoother in the TLS hillshade map than in the UAS-SfM map, only with some minor artifacts. The artifacts in the TLS data were most likely caused by the fact that they were so close to the AOI's boundary, resulting in a much lower point density in this area. The UAS-SfM, however, had adequate buffers captured to ensure the coverage of the AOI. Thus, the artifacts were mostly from a lack of matching key points caused by a dark and texture-less surface (figure 3.2). This was further proved by other segments such as 250 to 350 m and 400 to 500 m along the highway, where the UAS-SfM behaved similarly whereas the TLS resulted in a smooth surface where there was a strong correlation between the dark surface and rough artifacts of the DEM. Note also that even though overall the TLS accurately reflected the geometric characteristics of the road surface, regardless the color and material of the pavement, some artifacts occurred occasionally across the site (e.g., linear artifacts near 110 m along the highway). These were mostly caused by geo-referencing and registration errors between the TLS scans because of a number of factors such as GNSS errors, ranging errors, a lack of smooth surface serving as constraints in the point cloud alignment, and so on. All the aforementioned artifacts are highlighted and quantified in the difference map between the UAS-SfM and TLS DEMs (figure 3.1 (D)). In the following sections, the difference between the UAS-SfM and TLS DEMs are further analyzed quantitatively.

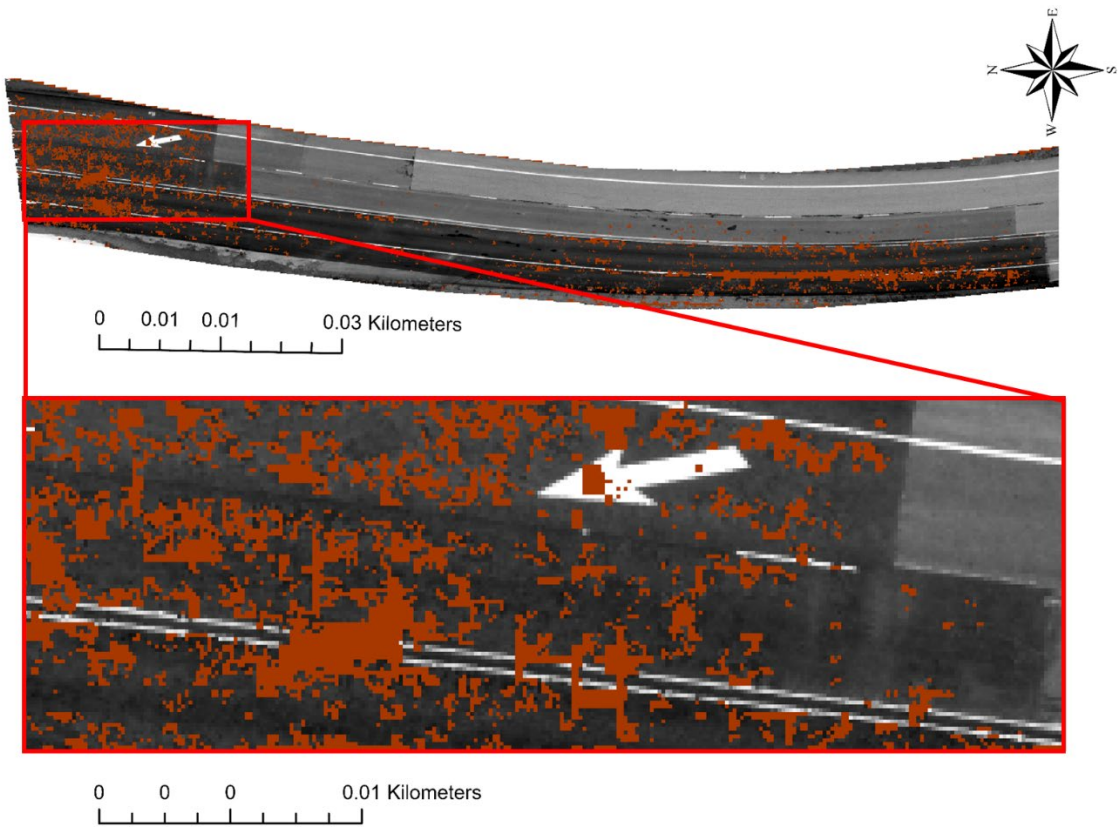

Figure 3.2. Close inspection of data gaps, where orange pixels represent the data gaps.

3.3. Lane Profile and IRI Comparison

The highway contained three lanes, and the research team generated two profiles from each lane for IRI assessment. First, the elevation difference between the UAS-SfM and TLS was summarized for each profile (table 3.2). As shown in the statistical analysis, the deviations shown from all the profiles were very consistent, as the average difference, standard deviation of difference, and root-mean-square deviation (RMSD) were around 0.01 m, 0.02 m, and 0.03 m, respectively. However, note that the maximum and minimum differences between two models showed substantially greater discrepancies. As discussed in the previous section, these large deviations were most likely a result of a dark and texture-less surface.

Table 3.2. Elevation difference analysis between the UAS-SfM and TLS data (unit: meters)

	Lane1_Left	Lane1_Right	Lane2_Left	Lane2_Right	Lane3_Left	Lane3_Right
Minimum	-0.137	-0.135	-0.138	-0.128	-0.089	-0.142
Maximum	0.059	0.055	0.054	0.063	0.061	0.077
Median	0.010	0.009	0.009	0.008	0.008	0.009
Average	0.011	0.011	0.012	0.011	0.011	0.011
Std. Deviation	0.021	0.022	0.021	0.022	0.021	0.022
RMSD	0.029	0.027	0.027	0.028	0.026	0.028

Then IRI values were computed along each profile from the UAS-SfM and TLS data. On the basis of the IRI values derived from the TLS data, the average IRI values were relatively consistent across all profiles. They ranged from 3.9 to 4.7 m/km, which was expected for most parts of the pavement. However, the average IRI values from the UAS-SfM data had significantly more variations and ranged from 7.5 to 11.4 m/km. Additionally, the IRI values from the UAS-SfM data were consistently higher than those from the TLS data, which indicated that the road surface in the UAS-SfM was rougher than in the TLS DEM. More noticeably, the difference between the profile elevations was clearly amplified and propagated to the IRI calculations, especially for the UAS-SfM data. For example, the maximum IRI values computed from the UAS-SfM data for all profiles ranged from 45.5 to 79.6 m/km, which indicated tremendous roughness. Nonetheless, despite of some variations in the maximum IRI values in the TLS data, they were much more consistent in comparison with the UAS-SfM data (ranging from 10.3 to 16.5 m/km), which could be largely explained by some localized differences between lanes and profiles. Then the differences in IRI computed from the TLS and UAS-SfM datasets were further reported statistically (table 3.3). Table 3.4 shows how the elevation differences in the profiles affected the IRI values. The average difference between the IRI values ranged between 2.9 and 7.6 m/km for each profile, which showed a clear bias in using the UAS-SfM data to estimate the IRI values. The RMSD also indicated both the biases and variations in the difference of IRI values, and it ranged from 9.0 to 13.7 m/km. Given the typical scale of the IRI measures (figure 1.1), the TLS-derived IRI indicated that the road was “Older Pavement” overall, with some sections that were “New Pavement” and “Damaged Pavement.” On the other hand, the IRI assessment from the UAS-SfM data indicated that the road was “Damaged Pavement” on average, with some “New Pavement” and some “Rough Unpaved Road.” In this case, the TLS-derived IRI values clearly depicted the road surface condition more accurately.

Table 3.3. Statistical summary of IRI values for each profile from the TLS and UAS-SfM data.

	Terrestial LIDAR Data IRI(m/km)					
(m/km)	Lane1_Left	Lane1_Right	Lane2_Left	Lane2_Right	Lane3_Left	Lane3_Right
Minimum	0.8	1.1	1.0	1.2	1.3	1.0
Maximum	11.1	11.0	10.3	14.1	11.9	16.5
Median	3.5	3.8	3.5	3.6	3.8	3.8
Average	3.9	4.1	3.8	4.3	4.4	4.6
	UAS-SfM Data IRI(m/km)					
Mimimum	1.9	2.2	2.0	2.0	1.8	2.1
Maximum	77.6	68.2	79.6	45.5	65.4	71.2
Median	7.0	6.5	6.4	4.5	4.2	4.6
Average	11.4	10.6	9.0	7.9	7.5	7.6

Table 3.4. Statistical summary of the IRI value difference (unit: m/km)

	Lane1_Left	Lane1_Right	Lane2_Left	Lane2_Right	Lane3_Left	Lane3_Right
Minimum	-3.1	-6.5	-5.3	-10.8	-9.8	-13.8
Maximum	69.7	58.6	69.6	41.3	57.8	67.5
Median	2.8	1.9	2.4	1.7	1.2	1.0
Average	7.6	6.5	5.1	3.6	3.1	2.9
Std. Deviation	11.4	11.5	9.1	8.3	8.6	10.2
RMSD	13.7	13.2	10.5	9.0	9.1	10.6

To further analyze how the IRI difference between the TLS and UAS-SfM data behaved and varied across the site, the differences between datasets were plotted in a graph (figure 3.3). First, note that some of the large discrepancies from the beginning and end of the profiles could have resulted from the artifacts near the boundary from both the data and the ProVAL software. Aside from those areas, most of the larger discrepancies occurred in three zones, whereas the differences in other areas were generally within 3 m/km. This showed that the IRI assessments from the TLS and UAS-SfM were on par with each other.

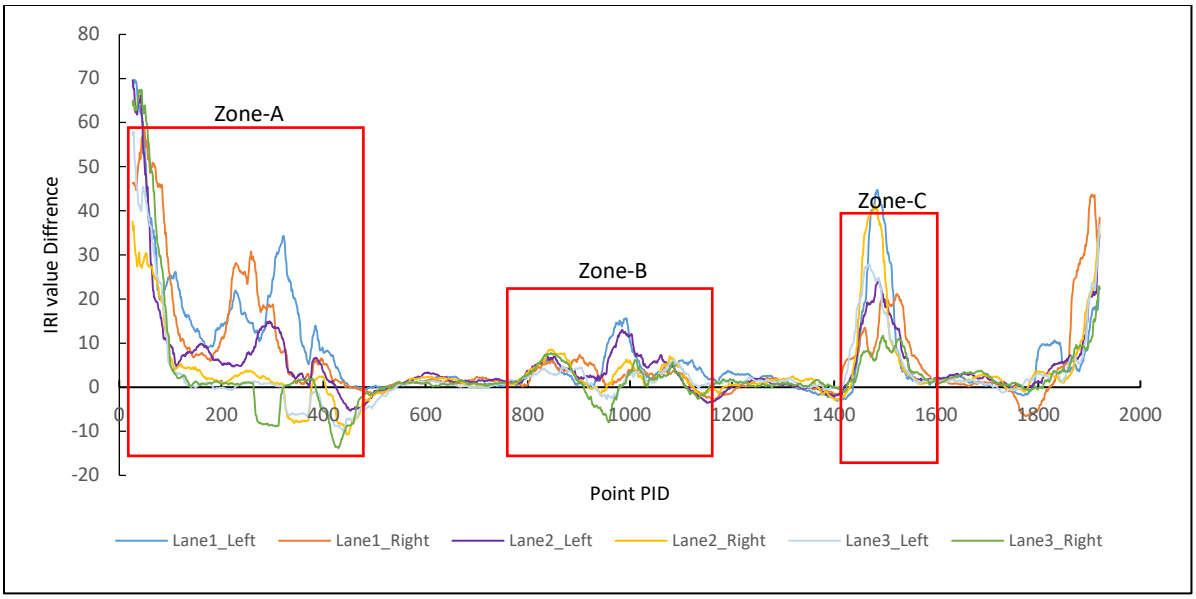

Figure 3.3. Differences between UAS-SfM- and TLS-derived IRI values

Then for those three zones (i.e., Zone A, Zone B, and Zone C) with large differences, more detailed analysis was carried out. As shown in the close-up views of the three zones (figure 3.4), they all featured large roughness caused by data gaps and errors, particularly where recently paved areas had a darker surface than other parts. To further quantify the impacts of such texture-less and dark surfaces on the IRI assessment, the research team extracted these subsections from the profiles and analyzed the differences in both elevations and IRI values statistically (table 3.5 and table 3.6). On the basis of the statistical analysis, there were large vertical variations in Zone A and Zone C, whereas there were no notable differences in vertical data in Zone B. The IRI difference in these zones followed the same trend in general. For Zone A and Zone B, the large discrepancy could be largely explained by the higher noise level and more data gaps in those areas. For Zone B, however, although the average, standard deviation, and RMSD of the elevations from the UAS-SfM data were on par with the accuracy of the TLS data, the UAS-SfM data still provided a higher estimation of IRI values. The fewer artifacts in Zone B can be explained by the facts that 1) Zone B had the smallest patch of very dark asphalt pavement, and 2) the irregular shape of the patch provided relatively more contrast to the image, which was essential for the 3D reconstruction process. That being said, there were still small data gaps in this section, and the gap filling algorithms could cope with this to generate a decent DEM. However, given the complexity of the surface itself, the assumptions made in the gap

filling and smoothing approaches could no longer accurately predict the actual surface characteristics.

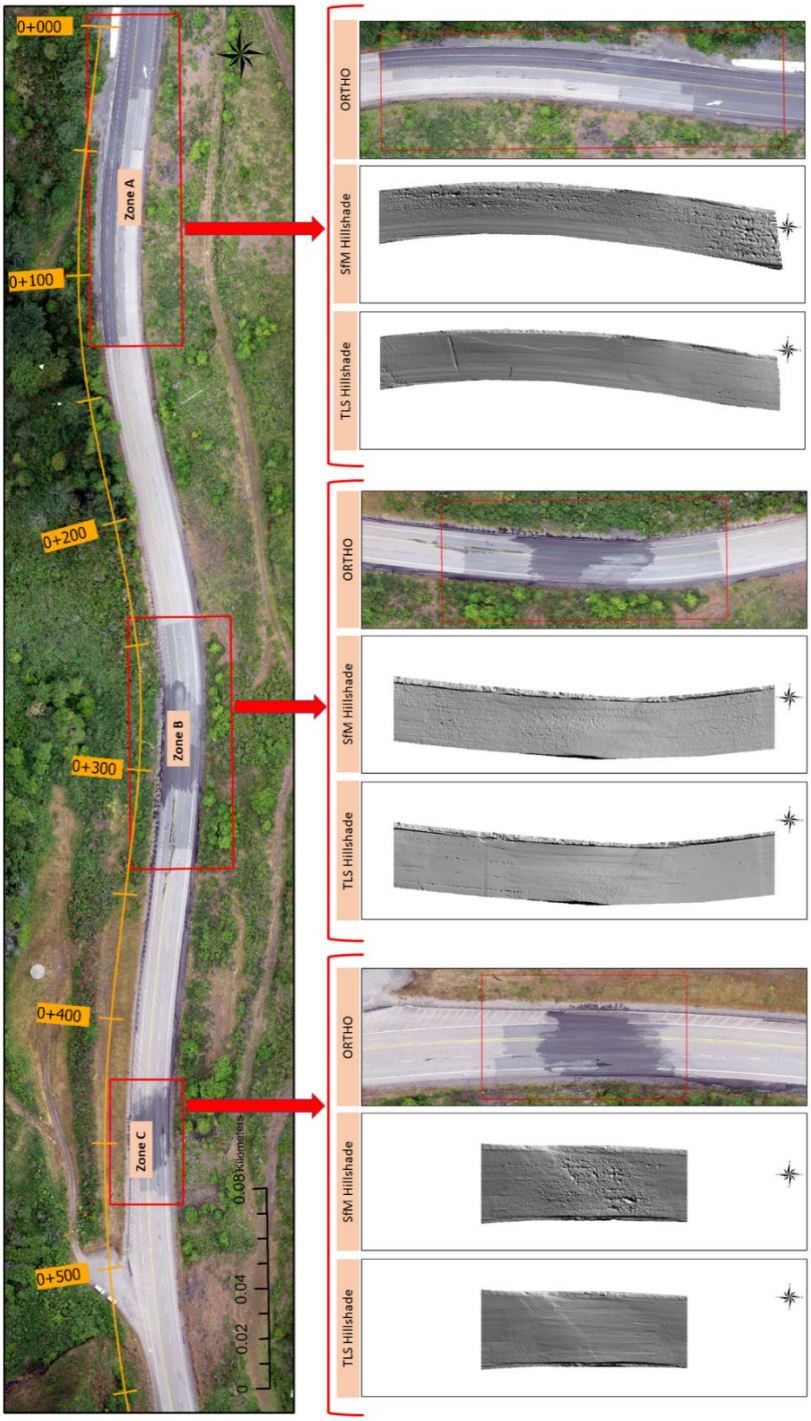

Figure 3.4. Close-up views of the zones that were newly paved with asphalt.

Table 3.5. Elevation differences by zones (unit: meters)

		Lane1_Left	*Lane1_Right*	*Lane2_Left*	*Lane2_Right*	*Lane3_Left*	*Lane3_Right*
Zone A	***Minimum***	-0.137	-0.135	-0.138	-0.128	-0.076	-0.123
	Maximum	0.035	0.029	0.043	0.042	0.036	0.077
	Median	0.003	0.002	0.003	0.001	0.001	0.000
	Average	-0.001	-0.001	0.001	-0.001	-0.001	-0.004
	Std. Deviation	0.023	0.019	0.017	0.018	0.016	0.019
	RMSD	0.023	0.019	0.017	0.018	0.016	0.019
Zone B	***Minimum***	-0.021	-0.031	-0.024	-0.027	-0.023	-0.026
	Maximum	0.038	0.032	0.039	0.031	0.026	0.034
	Median	0.010	0.008	0.009	0.010	0.010	0.011
	Average	0.007	0.006	0.007	0.007	0.007	0.008
	Std. Deviation	0.014	0.013	0.012	0.011	0.011	0.011
	RMSD	0.015	0.014	0.014	0.013	0.013	0.014
Zone C	***Minimum***	-0.086	-0.025	-0.022	-0.067	-0.046	-0.001
	Maximum	0.059	0.055	0.050	0.063	0.061	0.049
	Median	0.032	0.033	0.032	0.032	0.029	0.029
	Average	0.027	0.032	0.031	0.028	0.026	0.030
	Std. Deviation	0.020	0.011	0.011	0.016	0.016	0.008
	RMSD	0.034	0.034	0.034	0.033	0.031	0.032

Table 3.6. IRI value differences by zones (unit: m/km)

		Lane1_Left	*Lane1_Right*	*Lane2_Left*	*Lane2_Right*	*Lane3_Left*	*Lane3_Right*
Zone A	***Minimum***	3.7	0.8	-1.2	-8.3	-8.8	-13.8
	Maximum	69.5	58.3	69.5	37.7	57.8	67.8
	Median	16.3	11.1	7.6	2.4	0.6	0.8
	Average	20.2	17.8	12.0	5.0	5.1	7.0
	Std. Deviation	14.1	15.9	14.8	10.3	14.6	20.3
	RMSD	24.6	23.9	19.1	11.4	15.4	21.4
Zone B	***Minimum***	0.2	-1.0	-1.8	-1.9	-2.6	-7.7
	Maximum	15.6	7.3	13.0	8.5	6.3	7.6
	Median	4.4	3.4	4.8	3.6	3.0	2.4
	Average	5.1	3.3	4.9	3.5	2.5	1.8
	Std. Deviation	3.8	1.8	3.3	2.6	2.1	3.7
	RMSD	6.4	3.7	5.9	4.4	3.2	4.1
Zone C	***Minimum***	-2.7	1.4	-2.0	-2.4	-0.4	-1.3
	Maximum	44.8	21.4	24.2	41.3	27.7	11.8
	Median	5.7	9.2	9.6	7.1	8.6	6.4
	Average	14.3	11.2	10.1	13.6	11.4	5.8
	Std. Deviation	16.1	5.9	7.8	15.1	9.3	3.7
	RMSD	21.5	12.7	12.7	20.3	14.7	6.8

CHAPTER 4. CONCLUSIONS AND RECOMENDATIONS

This research developed a framework for collecting and processing UAS-SfM data to extract pavement information, and it examined the feasibility of employing UAS-derived point clouds to evaluate pavement roughness. The proposed framework consists of data acquisition, data processing, and IRI computations. A rigorous accuracy assessment and analysis were conducted. First, the research team evaluated the absolute accuracy of the UAS-SfM DEM against the results of a total station survey, including where the RMSE was 0.019 m among 180 check points along the study area. Then the UAS-SfM DEM was further compared to the DEM generated from TLS data along a number of profiles, and the RMSDs were consistently under 0.03 m. Furthermore, the difference in the IRI values along these profiles from the TLS and UAS-SfM data were compared. The results showed that dark and texture-less surface (e.g., asphalt) could result in significant vertical errors and data gaps, leading to unreliable IRI readings. On the other hand, for other parts of the road surface with brighter color, the UAS-SfM data slightly over-estimated the roughness of the road surface (generally within 3 m/km) in comparison to the results from the TLS data. Therefore, the researchers concluded that UAS-SfM can be a great technique for road surface roughness assessment, with some restrictions related to the material of the pavement. The findings from this experiment are valuable not only to surface roughness assessment but also to other projects that utilize UAS-SfM for accurate 3D representations of a subject.

The research team would also like to present the following highlights and recommendations:

- UASs provide additional data on surrounding features, as expected from an air-based vehicle with a large field-of-view; therefore, the collected data can be used for more comprehensive analysis and other applications.
- It is challenging for the SfM technique to reconstruct 3D information on dark and texture-less surfaces such as newly paved asphalt.
- Relatively small elevation derivations may have a massive effect on the IRI analysis. Localized analysis is recommended if abnormal IRI values are spotted.
- The ProVAL software needs about a 20-m buffer from beginning and ending of the profile data.

The research team plans to tackle the following tasks in the future:

- Test whether the artifacts in the UAS-SfM data can be mitigated by different flight planning and data acquisition strategies
- Compare the UAS-SfM point clouds generated from different software and settings, as well as their derivative roughness assessment results
- Investigate the impacts of different DEM parameters and hole filling techniques.

REFERENCES

Alhasan, A. A., Younkin, K., & White, D. J. (2015). Comparison of roadway roughness derived from lidar and sfm 3d point clouds.

Agüera-Vega, F., Carvajal-Ramírez, F., & Martínez-Carricondo, P. (2017). Assessment of photogrammetric mapping accuracy based on variation ground control points number using unmanned aerial vehicle. *Measurement*, *98*, 221-227.

ASTM E1926-08. (Reapproved 2021). Standard practice for computing international roughness index of roads from longitudinal profile measurements. *West Conshohocken, PA: ASTM International*.

Authority, T. V. (1998). Geospatial Positioning Accuracy Standards Part 3: National Standard for Spatial Data Accuracy. *National Aeronautics and Space Administration: Virginia, NV, USA*.

Barbarella, M., D'Amico, F., De Blasiis, M. R., Di Benedetto, A., & Fiani, M. (2017). Use of terrestrial laser scanner for rigid airport pavement management. *Sensors, 18*(1), 44.

Bennett, C. R., De Solminihac, H., & Chamorro, A. (2006). Data collection technologies for road management.

Che, E., Jung, J., & Olsen, M. J. (2019). Object recognition, segmentation, and classification of mobile laser scanning point clouds: A state of the art review. *Sensors*, *19*(4), 810.

Che, E., Senogles, A., & Olsen, M. J. (2021). Vo-SmoG: A Versatile, Smooth Segment-based Ground Filter for Point Clouds via Multi-scale Voxelization. *ISPRS Annals of the Photogrammetry, Remote Sensing and Spatial Information Sciences, 8*, 59-66.

Cruz, O. G. D., Mendoza, C. A., & Lopez, K. D. (2021). *International Roughness Index as Road Performance Indicator: A Literature Review.* Paper presented at the IOP Conference Series: Earth and Environmental Science.

De Blasiis, M. R., Di Benedetto, A., & Fiani, M. (2020). Mobile laser scanning data for the evaluation of pavement surface distress. *Remote Sensing, 12*(6), 942.

De Blasiis, M. R., Di Benedetto, A., Fiani, M., & Garozzo, M. (2020). Assessing of the road pavement roughness by means of LiDAR technology. *Coatings, 11*(1), 17.

Dobson, R. J., Brooks, C., Roussi, C., & Colling, T. (2013). *Developing an unpaved road assessment system for practical deployment with high-resolution optical data collection using a helicopter UAV.* Paper presented at the 2013 International Conference on Unmanned Aircraft Systems (ICUAS).

Elghriany, A., Yi, P., Liu, P., & Yu, Q. (2016). Investigation of the effect of pavement roughness on crash rates for rigid pavement. *Journal of Transportation Safety & Security, 8*(2), 164-176.

Fakhri, M., Karimi, S. M., & Barzegaran, J. (2021). Predicting international roughness index based on surface distresses in various climate and traffic conditions using laser crack measurement system. Transportation Research Record, 2675(11), 397-412.

Fonstad, M. A., Dietrich, J. T., Courville, B. C., Jensen, J. L., & Carbonneau, P. E. (2013). Topographic structure from motion: a new development in photogrammetric measurement. *Earth surface processes and Landforms, 38*(4), 421-430.

Greenwood, W. W., Lynch, J. P., & Zekkos, D. (2019). Applications of UAVs in civil infrastructure. *Journal of infrastructure systems, 25*(2), 04019002.

Hurwitz, D. S., Olsen, M. J., & Barlow, Z. (2018). *Driving Distraction Due to Drones* (No. FHWA-OR-RD-18-12). Oregon. Dept. of Transportation. Research Section.

Iglhaut, J., Cabo, C., Puliti, S., Piermattei, L., O'Connor, J., & Rosette, J. (2019). Structure from motion photogrammetry in forestry: A review. *Current Forestry Reports, 5*(3), 155-168.

Inzerillo, L., Di Mino, G., & Roberts, R. (2018). Image-based 3D reconstruction using traditional and UAV datasets for analysis of road pavement distress. *Automation in Construction, 96*, 457-469.

Javadnejad, F., Slocum, R. K., Gillins, D. T., Olsen, M. J., & Parrish, C. E. (2021). Dense point cloud quality factor as proxy for accuracy assessment of image-based 3D reconstruction. *Journal of Surveying Engineering, 147*(1), 04020021.

Karamihas, S. (2021). *Improvement of Inertial Profiler Measurements of Urban and Low-Speed Roadways.*

Lee, M. H., & Chou, C. P. (2010). Laboratory method for inertial profiler verification. *Journal of the Chinese Institute of Engineers, 33*(4), 617-627.

Liao, Y., & Wood, R. L. (2020). Discrete and Distributed Error Assessment of UAS-SfM Point Clouds of Roadways. *Infrastructures, 5*(10), 87.

Loizos, A., & Plati, C. (2008). An alternative approach to pavement roughness evaluation. *International Journal of Pavement Engineering, 9*(1), 69-78.

Louhghalam, A., Akbarian, M., & Ulm, F.-J. (2015). Roughness-induced pavement–vehicle interactions: key parameters and impact on vehicle fuel consumption. *Transportation Research Record, 2525*(1), 62-70.

Múčka, P. (2017). International Roughness Index specifications around the world. *Road Materials and Pavement Design, 18*(4), 929-965.

Nappo, N., Mavrouli, O., Nex, F., van Westen, C., Gambillara, R., & Michetti, A. M. (2021). Use of UAV-based photogrammetry products for semi-automatic detection and classification of asphalt road damage in landslide-affected areas. *Engineering geology, 294*, 106363.

Olsen, M. J. (2013). *Guidelines for the use of mobile LIDAR in transportation applications* (Vol. 748): Transportation Research Board.

Olsen, M. J., & Gillins, D. T. Influence of coordinate system selection for coastal deformation analyses.

Olsen, M. J., Johnstone, E., Driscoll, N., Ashford, S. A., & Kuester, F. (2009). Terrestrial laser scanning of extended cliff sections in dynamic environments: Parameter analysis. *Journal of Surveying Engineering, 135*(4), 161-169.

Olsen, M. J., Wartman, J., McAlister, M., Mahmoudabadi, H., O'Banion, M. S., Dunham, L., & Cunningham, K. (2015). To fill or not to fill: sensitivity analysis of the influence of resolution and hole filling on point cloud surface modeling and individual rockfall event detection. *Remote Sensing, 7*(9), 12103-12134.

Olsen, M. J., & Chin, A. (2012). *Inertial and inclinometer based profiler repeatability and accuracy using the IRI model*. Retrieved from

Ong, G. P. R., Noureldin, S., & Sinha, K. C. (2010). Automated pavement condition data collection quality control, quality assurance, and reliability.

Prosser-Contreras, M., Atencio, E., Muñoz La Rivera, F., & Herrera, R. F. (2020). Use of unmanned aerial vehicles (UAVs) and photogrammetry to obtain the International roughness Index (IRI) on roads. *Applied Sciences, 10*(24), 8788.

Radović, N., Jokanović, I., Matić, B., & Šešlija, M. (2016). A measurement of roughness as indicator of road network condition–case study Serbia. *Technical Gazette, 23*(3).

Ragnoli, A., De Blasiis, M. R., & Di Benedetto, A. (2018). Pavement distress detection methods: A review. *Infrastructures, 3*(4), 58.

Romero-Chambi, E., Villarroel-Quezada, S., Atencio, E., & Muñoz-La Rivera, F. (2020). Analysis of optimal flight parameters of unmanned aerial vehicles (UAVs) for detecting potholes in pavements. *Applied Sciences*, *10*(12), 4157.

Saad, A. M., & Tahar, K. N. (2019). Identification of rut and pothole by using multirotor unmanned aerial vehicle (UAV). *Measurement, 137*, 647-654.

Sayers, M. W. (1986). *Guidelines for conducting and calibrating road roughness measurements*. Retrieved from

Sayers, M. W. (1989). Two quarter-car models for defining road roughness: IRI and HRI. *Transportation Research Record*(1215).

Sayers, M. W. (1995). On the calculation of international roughness index from longitudinal road profile. Transportation Research Record, (1501).Sayers, M. W. (1998). The little book of profiling: basic information about measuring and interpreting road profiles.

Sayers, M. W., & Karamihas, S. M. (1997). *ERD file format for storage and analysis of road profiles*. Retrieved from

Schnebele, E., Tanyu, B., Cervone, G., & Waters. (2015). Review of remote sensing methodologies for pavement management and assessment. *European Transport Research Review, 7*(2), 1-19.

Shan, J., & Toth, C. K. (2018). *Topographic laser ranging and scanning: principles and processing*: CRC press.

Simpson, C. H. (2018). A multivariate comparison of drone-based structure from motion and drone-based lidar for dense topographic mapping applications.

Slocum, R. K. and Parrish, C. E. (2017) 'Simulated Imagery Rendering Workflow for Accuracy Assessments UAS-based Photogrammetric 3D Reconstruction Accuracy Assessments', *Remote Sensing*, 9(4), p. 396. doi: 10.3390/rs9040396.

Smith, K. D., & Ram, P. (2016). *Measuring and Specifying Pavement Smoothness:[techbrief]*. Retrieved from

Šroubek, F., Šorel, M., & Žák, J. (2021). Precise international roughness index calculation. International Journal of Pavement Research and Technology, 1-7.

Tan, Y., & Li, Y. (2019). UAV photogrammetry-based 3D road distress detection. ISPRS International Journal of Geo-Information, 8(9), 409.

Thomas, F. (2021). *Can the method for calculating the International Roughness Index used by the company Infrafocus be certified according to Dutch regulations?* University of Twente,

Transtec Group. (2015). ProVAL Software: View and Analyze Pavement Profiles. *ProVAL Website.* Retrieved from https://www.thetranstecgroup.com/portfolio-items/proval-software-view-and-analyze-pavement-profiles/

Transtec Group. (2016). ProVAL user's guide, version 3.6. In: The Transtec Group Austin, TX.

Varbla, S., Ellmann, A., & Puust, R. (2021). Centimetre-range deformations of built environment revealed by drone-based photogrammetry. *Automation in Construction, 128*, 103787.

Vosselman, G., & Maas, H.-G. (2010). *Airborne and terrestrial laser scanning*: CRC press.

Voumard, J., Derron, M.-H., Jaboyedoff, M., Bornemann, P., & Malet, J.-P. (2018). Pros and Cons of Structure for Motion Embarked on a Vehicle to Survey Slopes along

Transportation Lines Using 3D Georeferenced and Coloured Point Clouds. *Remote Sensing, 10*(11), 1732.

Ward, A. B., & Newman, J. K. (2019). *Assessment of LiDAR and Photogrammetry based Airfield Roughness Profiling Techniques*. Retrieved from

White, R. A., Dietterick, B. C., Mastin, T., & Strohman, R. (2010). Forest roads mapped using LiDAR in steep forested terrain. *Remote Sensing, 2*(4), 1120-1141.

Zeybek, M., & Biçici, S. (2021). 3D Dense Reconstruction of Road Surface from UAV Images and Comparison of SfM Based Software Performance. *Turkish Journal of Remote Sensing and GIS, 2*(2), 96-105.

BIBLIOGRAPHY

Atencio, E., Plaza-Muñoz, F., Muñoz-La Rivera, F., & Lozano-Galant, J. A. (2022). Calibration of UAV flight parameters for pavement pothole detection using orthogonal arrays. *Automation in Construction, 143*, 104545.

Babbel, B. J., Olsen, M. J., Che, E., Leshchinsky, B. A., Simpson, C., & Dafni, J. (2019). Evaluation of uncrewed aircraft systems' LiDAR data quality. *ISPRS International Journal of Geo-Information, 8*(12), 532.

Cabo, C., Cortés, S. G., & Ordoñez, C. (2015). Mobile Laser Scanner data for automatic surface detection based on line arrangement. *Automation in Construction, 58*, 28-37.

De Blasiis, M. R. D., Benedetto, A. D., Fiani, M., & Garozzo, M. (2019). Assessing the effect of pavement distresses by means of LiDAR technology. In *Computing in civil engineering 2019: Smart cities, sustainability, and resilience* (pp. 146-153): American Society of Civil Engineers Reston, VA.

Duffell, C., & Rudrum, D. (2005). Remote sensing techniques for highway earthworks assessment. In *Site Characterization and Modeling* (pp. 1-13).

Duffy, J. P., Cunliffe, A. M., DeBell, L., Sandbrook, C., Wich, S. A., Shutler, J. D., . . . Anderson, K. (2018). Location, location, location: considerations when using lightweight drones in challenging environments. *Remote Sensing in Ecology and Conservation, 4*(1), 7-19.

Gong, J., Zhou, H., Gordon, C., & Jalayer, M. (2012). Mobile terrestrial laser scanning for highway inventory data collection. *Computing in civil engineering, 2012*, 545–552.

Jacob-Loyola, N., Muñoz-La Rivera, F., Herrera, R. F., & Atencio, E. (2021). Unmanned aerial vehicles (UAVs) for physical progress monitoring of construction. *Sensors, 21*(12), 4227.

James, M. R., Robson, S., & Smith, M. W. (2017). 3-D uncertainty-based topographic change detection with structure-from-motion photogrammetry: precision maps for ground control and directly georeferenced surveys. *Earth surface processes and Landforms, 42*(12), 1769-1788.

Lovas, T., Baranyai, D., & Somogyi, Á. (2022). *Point Cloud Based Road Surface Modelling and Assessment.* Paper presented at the The First Conference on ZalaZONE Related R&I Activities of Budapest University of Technology and Economics 2022.

O'Banion, M. S., & Olsen, M. J. (2018). Efficient planning and acquisition of terrestrial laser scanning–derived digital elevation models: Proof of concept study. *Journal of Surveying Engineering, 145*(1), 06018003.

O'Banion, M. S., Olsen, M. J., Hollenbeck, J. P., & Wright, W. C. (2020). Data Gap Classification for Terrestrial Laser Scanning-Derived Digital Elevation Models. *ISPRS International Journal of Geo-Information, 9*(12), 749.

Pradhan, B., & Sameen, M. I. (2020). *Laser scanning systems in highway and safety assessment*: Springer.

Puente[a], I., González-Jorge[a], H., Arias[a], P., & Armesto[a], J. (2011). Land-based mobile laser scanning systems: A review. *International archives of the photogrammetry, remote sensing and spatial information sciences, 38*(5/W12).

Schwendel, A. C., & Milan, D. J. (2020). Terrestrial structure-from-motion: Spatial error analysis of roughness and morphology. *Geomorphology, 350*, 106883.

Wang, Y., & Madani, M. (2004). Automatic detection of shadow points in digital images for automatic triangulation. *International archives of the photogrammetry, remote sensing and spatial information sciences, 35*.

Wheeler, P. (2019). *Use of Small Unmanned Aerial Systems for Land Surveying*. Retrieved from

Williams, K., Olsen, M. J., Roe, G. V., & Glennie, C. (2013). Synthesis of transportation applications of mobile LiDAR. *Remote Sensing, 5*(9), 4652-4692.

Yan, W. Y., Shaker, A., & El-Ashmawy, N. (2015). Urban land cover classification using airborne LiDAR data: A review. *Remote Sensing of Environment, 158*, 295-310.

Zampa, F., & Conforti, D. (2009). Mapping with mobile lidar. *GIM international, 23*(4), 35-37.

APPENDIX A

Poster for 3D GeoInfo 2021 Conference:

Assessing the Feasibility of Utilizing UAS-based Point Cloud in Pavement Smoothness/Roughness Measurement

Fatih Sen,[1] Erzhuo Che,[1] Chase Simpson[1]

1. School of Civil and Construction Engineering, Oregon State University

BACKGROUND

The driving quality and highway safety are critical quality indicators that transportation agencies are continuously striving to improve and are highly correlated with the smoothness of the road. To standardize the smoothness/roughness metrics, the International Roughness Index (IRI), calculated from longitudinal profile data collected on the road, was widely adopted. Structure of Motion (SfM) approach has lately been extensively utilized owing to their ability to reconstruct 3D information of structures and the associated textures. Especially, the uncrewed aircraft system (UAS) is highly efficient in gathering rich information in a local area. The core question regarding this method is whether the point clouds generated with such techniques can be utilized for measuring the pavement roughness (e.g., IRI) with sufficient accuracy. To answer this question, this study aims to establish a framework to attain IRI metrics from point cloud and assess its accuracy.

WORKFLOW

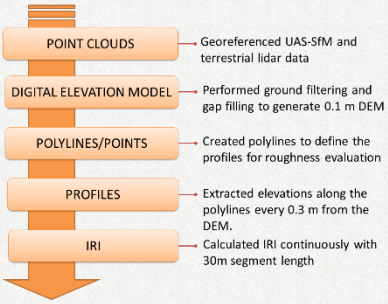

DATA COLLECTION

The project was carried out in southern Oregon coast along U.S. Highway 101 where there is an active landslide, named Arizona Inn. A control network was established with 10 ground control points (GCPs) set up along the shoulders surrounding the targeted road section. UAV-SfM data acquisition was performed with DJI-Phantom 4 RTK at 48.8m flight altitude. Additionally, 1062 image were collected with 1.36cm/pix ground resolution. Additionally, a total of 17 terrestrial lidar scans with images were collected using Riegl VZ-400 to cover road section of interest, which served as reference in the following analysis.

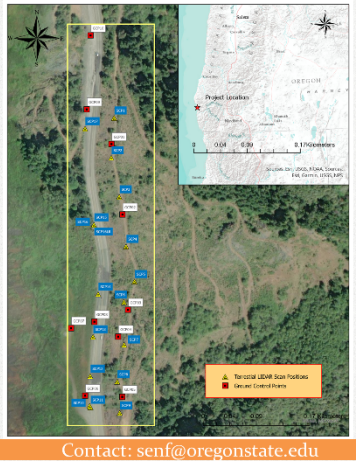

RESULTS & ANALYSIS

ELEVATION DIFFERENCECES

(m)	Profile 1	Profile 2	Profile 3	Profile 4	Profile 5	Profile 6
MIN	-0.018	-0.074	-0.013	-0.044	-0.007	-0.011
MAX	0.084	0.075	0.086	0.151	0.103	0.083
MEDIAN	0.020	0.022	0.021	0.020	0.021	0.021
MEAN	0.020	0.020	0.020	0.020	0.020	0.021
STD.DEV	0.019	0.019	0.019	0.019	0.018	0.018

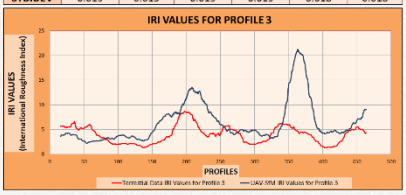

IRI VALUES DIFFERENCES

(m/km)	Profile 1	Profile 2	Profile 3	Profile 4	Profile 5	Profile 6
MIN	-3.11	-1.38	-3.52	-7.91	-4.84	-6.70
MAX	9.84	28.19	16.65	19.75	10.70	6.86
MEDIAN	1.92	2.02	1.72	1.18	1.05	2.39
MEAN	2.77	3.44	2.44	1.83	1.22	1.77
STD.DEV	3.20	4.81	3.80	4.66	2.68	2.68

REFERENCES

[1] ASTM. (E1926 – 08 (Reapproved 2021)). *Standard Practice for Computing International Roughness Index of Roads from Longitudinal Profile Measurements* (Vol. 04.03). ASTM International.

Contact: senf@oregonstate.edu

APPENDIX B

Poster for 2022 Region 10 Transportation Conference:

School of Civil and Construction Engineering

ASSESSING THE ACCURACY AND FEASIBILITY OF UTILIZING UAS-BASED POINT CLOUD IN PAVEMENT SMOOTHNESS/ROUGHNESS MEASUREMENT

Fatih Sen, Erzhuo Che, Chase Simpson

Oregon State University

BACKGROUND

The driving quality and highway safety are critical quality indicators that transportation agencies are continuously striving to improve and are highly correlated with the smoothness of the road. To standardize the smoothness (or) roughness metrics, the International Roughness Index (IRI), calculated from longitudinal profile data collected on the road, was widely adopted. Structure of Motion (SfM) approach has lately been extensively utilized owing to their ability to reconstruct 3D information of structures and the associated textures. Especially, the uncrewed aircraft system (UAS) is highly efficient in gathering rich information in a local area. The core question regarding this method is whether the point clouds generated with such techniques can be utilized for measuring the pavement roughness (e.g., IRI) with sufficient accuracy. To answer this question, this study aims to establish a framework to attain IRI metrics from point cloud and assess its accuracy.

DATA COLLECTION

The project was carried out in southern Oregon coast along U.S. Highway 101 where there is an active landslide, named Arizona Inn. A control network was established with 10 ground control points (GCPs) set up along the shoulders surrounding the targeted road section. UAV-SfM data acquisition was performed with DJI-Phantom 4 RTK at 48.8m flight altitude. Additionally, 1062 image were collected with 1.36 cm/pix ground resolution. Additionally, a total of 17 terrestrial lidar scans with images were collected using Riegl VZ-400 to cover road section of interest, which served as reference in the following analysis.

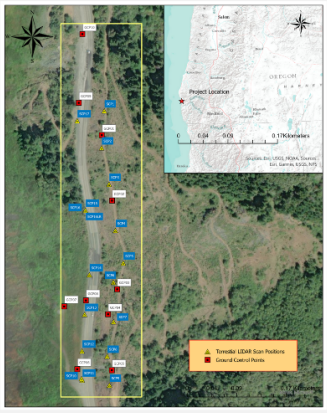

WORKFLOW

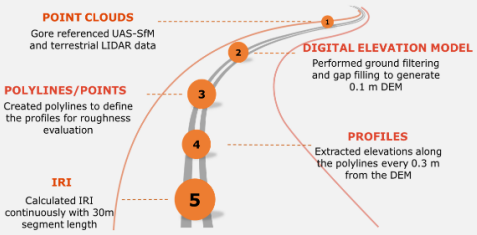

RESULT & ANALYSIS

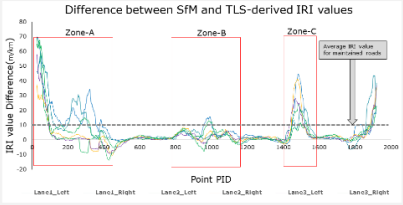

Statistical Summary of the IRI Value Comparison (m/km)						
	Lane 1 Left	Lane 1 Right	Lane 2 Left	Lane 2 Right	Lane 3 Left	Lane 3 Right
Minimum	-3.1	-6.5	-5.3	-10.8	-9.8	-13.8
Maximum	69.7	58.6	69.6	41.3	57.8	67.5
Median	2.8	1.9	2.4	1.7	1.2	1.0
Average	7.6	6.5	5.1	3.6	3.1	2.9
STD. Dev	11.4	11.5	9.1	8.3	8.6	10.2

ZONE-A

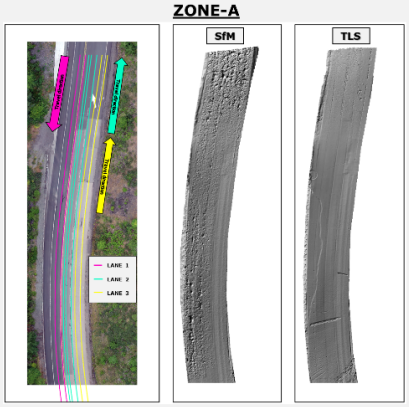

Note: Left/right definitions of the lanes are set with respect to travel direction

Statistical Summary of the IRI Value Comparison for Zone-A (m/km)						
	Lane 1 Left	Lane 1 Right	Lane 2 Left	Lane 2 Right	Lane 3 Left	Lane 3 Right
Minimum	3.7	0.8	-1.2	-8.3	-8.8	-13.8
Maximum	69.5	58.3	69.5	37.7	57.8	67.8
Median	16.3	11.1	7.6	2.4	0.6	0.8
Average	20.2	17.8	12.0	5.0	5.1	7.0
Std. Dev.	14.1	15.9	14.8	10.3	14.6	20.3

CHECK LANE

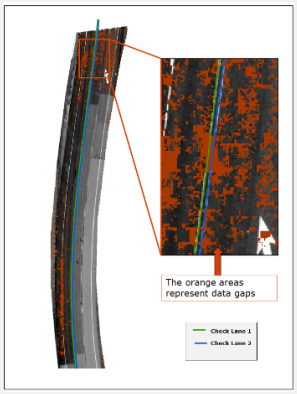

IRI Values Difference Statistics for Zone-A (m/km)		
	Check Lane 1	Check Lane 2
Minimum	0.0	-6.0
Maximum	99.5	38.8
Median	9.1	1.8
Average	22.4	4.3
Std. Dev.	26.8	9.7

CONCLUSION

Lesson learned

- Texture has a direct impact on SfM process and its derivative DEMs, which is why darker and texture-less surfaces have adverse effects on IRI computations.
- The IRI difference between SfM and TLS ranges from 2.9 to 7.6 (m/km) in this study. The standard deviations, another aspect of accuracy, are high due to the object texture, georefencing accuracy, ground filtering performance, and other factors,.
- To provide accurate estimates for smaller areas, the ProVAL requires a 20-meter buffer zone between the beginning and end of the project's AOI.

Future possibilities/ explorations

- The other zones(Zone B and Zone C) also needs to be investigated
- Re-investigate the check lane analysis with higher resolution SfM and TLS data